Integrated experimental and computational approach to simulation of flow in a stirred tank

H.S. Yoon[1], K.V. Sharp[2], D.F. Hill[3], R.J. Adrian[2], S. Balachandar[2*], M.Y. Ha[1], K. Kar[4]
[1]School of Mechanical Engineering, San 30 Chang Jeon Dong, Pusan National University, S. Korea
[2]Department of Theoretical & Applied Mechanics, 216 Talbot Lab, University of Illinois, Urbana, IL, 61801
[3]Department of Civil & Environmental Engineering, 212 Sackett Building, Pennsylvania State University, University Park, PA, 16802
[4]Dow Chemical Company, 1776 Dow Center, Midland, MI, 48674

Abstract

The stirred tank reactor is one of the most commonly used devices in industry for achieving mixing and reaction. We consider a combined experimental/computational approach for the simulation of flow inside a stirred tank. Two sets of experiments are performed to measure the velocity field in the neighborhood of the impeller. The first set of PIV measurements are on six different r-z planes phase locked at 0°, 10°, 20°, 30°, 40° and 50° to the blade location. The second set of PIV measurements is on a curved θ-z plane whose radial location is just outside the impeller blade tip radius. Measurements indicate that the impeller induced flow is dominated by three flow components: a circumferential flow, a tangential jet and pairs of tip vortices. A simple theoretical model is developed for each flow component and their superposition is observed to provide a good description of the impeller induced flow. The theoretical model is used as a velocity boundary condition for numerical simulation. The impeller induced boundary condition is fully three-dimensional, an important aspect that significantly enriches the mathematical representation of the primary source of motion. The results of two-dimensional and three-dimensional simulations are compared with measurements in the interior of the tank.

Keywords: Rushton turbine, turbulence, simulation, mixing, fluid mechanics, particle image velocimetry

* Corresponding Author, Phone: 217-244-4371, Fax: 217-244-9090, email: s-bala@uiuc.edu.

1. Introduction

A stirred tank reactor is one of the most commonly used devices in industry for achieving mixing and heat & mass transfer. Even a simple stirred tank is geometrically complex due to the presence of one or more impellers. Furthermore, under most operating conditions the flow is fully turbulent. The flow is often turbulent over the entire tank; the spatio-temporal complexity of the flow is not limited to the vicinity of the impellers (Rao & Broadkey 1972). As a result, prediction of flow and mixing in a stirred tank is challenging.

One of the fundamental challenges in the design of stirred tank reactors is to transfer the process technology from the laboratory-scale experiments of a few liters to production-scale stirred tanks of several thousand liters. For lack of a reliable approach to guide the scale-up process, the design of a production-scale stirred tank often evolves through a number of intermediate stages involving a series of larger and larger laboratory experiments and pilot plants. This time consuming and expensive step-by-step scale-up process is currently necessary to build confidence in the final product. Without further advances in the development of a reliable computational tool, the design of stirred tank reactors will continue to contain uncertainties that can be removed only by recourse to expensive experimental verification and pilot plants.

Development of a reliable computational approach for the design of stirred tank reactors faces an important challenge: incorporation of the effects of the impellers. There have been recent attempts at computing the detailed flow around the impellers using moving/deforming grids and sliding meshes (Luo, Gosman, Issa, Middleton & Fitzgerald 1993 and Lee, Ng & Yianneskis 1996). This approach may be viable at low Reynolds numbers corresponding to slow operating speeds in a small tank of very viscous fluid. However, at higher Reynolds numbers the flow in the impeller region is quite complex, and the range of length and time scales is so wide as to preclude direct numerical simulation of all these scales. Even large eddy simulation faces a severe challenge in the impeller region. First, the geometry of the impeller is far too complex for accurate and complete representation. Unlike eddies in the turbulent cascade in the bulk of the tank, in the region close to the impeller the eddies are driven directly by external driving mechanism; they are thus *problem-dependent* and cannot be represented by a universal model.

Instead of a direct computation of the impeller-induced flow, the effect of the impellers can be incorporated into the computations as distributed momentum source experiments s (Eggels 1996 and Revstedt, Fuchs & Tragardh 1998) or through an approximate aerodynamic theory for the impeller blades

(Pericleous & Patel 1987). The strength and spatial distribution of momentum sources are not known *a priori*. In the present work, we address the flow in a stirred tank through a coordinated experimental and computational effort. Particle image velocimetry (PIV) (Sharp, Kim & Adrian 1999) and stereoscopic PIV experiments (Hill, Sharp & Adrian 2000) are performed to obtain detailed information on the velocity field in the neighborhood of the impeller. Then, computation of the flow is performed outside of the impeller swept volume (see figure 1). This procedure generalizes past computations of stirred tank flow, where in the average velocity on a pillbox around the impeller obtained from an experimental measurements has been used as boundary condition (Ranade & Joshi 1989 and Ju, Mulvahill & Pike 1990). In the present work a three-component velocity field is obtained around the impeller region using stereo PIV, thus providing a more-realistic complex three-dimensional impeller-induced flow as input for the computations.

Accurate measurement of the velocity field around the impeller swept volume alone is not sufficient for successful interfacing with the computations. A good theoretical model for the impeller-induced flow is required in order to cast the experimental measurement into a meaningful velocity boundary condition for the computations. Based on the experimental measurements, a simple theoretical description of the impeller-induced flow is developed. Results suggest that the flow induced from the Rushton turbine can be described as a superposition of a circumferential flow, a tangential jet and a pair of tip vortices associated with each impeller blade (see Kolar, Filip & Curev 1982, 1984, Kresta & Wood 1991, Placek & Tavlarides 1985). The impeller-induced flow is strongly three-dimensional, and as a result a complex theoretical description is necessary to capture all the essential features. It must be emphasized that a simple curve-fit or naïve interpolation of the experimental data for application as boundary condition in the computations is futile.

It is important to assess the scaling behavior of the impeller-induced flow with parameters such as the size and rotational speed of the impeller. In practical application one cannot rely upon performing experiments each time velocity boundary conditions are needed at the impeller swept volume. The computations, after all, are intended to replace the expensive experimental scale-up. The scaling of the velocity boundary condition is complicated by the fact that the impeller-induced flow does not follow a simple scaling with the geometric and operating parameters. A good understanding of each physical mechanism at work in inducing the impeller flow is important in establishing an accurate overall scaling relation. An important advantage of the theoretical description is to simplify the scaling behavior. Each component of the impeller-induced flow (circumferential flow, circular jet and tip vortices) appears to follow a simple scaling law, which is evaluated from a limited set of experiments. However, the individual

scaling laws are different for the different components, thus explaining the lack of a simple scaling for the overall impeller-induced flow. Computations are also performed with these boundary conditions and the results on flow and turbulence in the interior of the tank (away from where boundary conditions are specified) are compared with those from experiments.

2. Experimental methodology

A schematic of the stirred tank with a single Rushton turbine having six impeller blades located midway between the top and bottom of the tank is shown in Figure 1 (turbine diameter D=50.8mm). This geometry is investigated computationally as well with appropriate boundary conditions on the circular surface of the impeller swept volume obtained from the experiments. Proper data-facing between the two is accomplished with a theoretical model for the impeller-induced flow. To best match the computations to be presented below a non-baffled tank is used for the present measurements.

The purposes of the present experiments are three fold: first to provide the necessary information for the development of accurate velocity boundary conditions on the circular surface of the impeller swept volume; second to obtain physical insights and justifications for modeling the impeller-induced flow on the circular boundary of the impeller swept volume in terms of identifiable flow mechanisms; and finally to establish a benchmark for the flow and mixing within the stirred tank against which the computational results can be compared for validation. In order to accomplish these objectives three sets of measurements were taken: 1) two-dimensional PIV measurements on r-z planes phase locked at 0°, 10°, 20°, 30°, 40° and 50° with respect to the blades. In this set of measurements the field of view is limited to the near blade region; 2) two-dimensional PIV measurements on r-z planes, similar to the first set but with a larger field of view; 3) stereoscopic PIV measurements on the θ-z surface of the impeller swept volume (radius $\approx D/2$) to obtain all three components of velocity on this cylindrical surface (Hill *et al.* 2000).

Figure 2 shows the experimental set-up for the r-z plane measurements. A pulsed Nd:Yag laser is used to illuminate the particles, providing a lightsheet in one r-z plane of the flow, where the velocity field is measured. The six blade Rushton turbine has a six fold symmetry in the azimuthal direction, so only 60° of phase-locked information is required to define the statistics of the entire flow. Here phase locked data is acquired in increments of 10° over the total 60° sector. One hundred pairs of images are acquired at each phase-locked blade position, from which 100 velocity fields are obtained. Two datasets are obtained with

magnifications 0.26 and 0.56. The lower magnification dataset has a field of view of 34.4mm by 34.7mm and the higher magnification has a field of view is 16.1mm by 16.2mm.

Samples of instantaneous velocity vector fields at the six different phase locked locations are shown in figure 3 for the smaller field of view. The measurements are taken at an impeller speed of 100 rpm which corresponds to a mixing Reynolds number of $\mathrm{Re} = \mathrm{N}D^2 / \nu = 4000$, where N is number of revolutions per second and ν is the kinematic viscosity of the fluid. The corresponding phase-average taken over 100 realizations is shown in figure 4. In this figure and in what follows, all quantities are nondimensional unless specified explicitly in dimensional terms. The tip radius ($D/2$) is taken as the length scale, the blade tip velocity (πND) is the velocity scale, the time and pressure scales are accordingly defined as ($1/2\pi N$) and ($\rho[\pi ND]^2$). In the strict sense there is no symmetry about the z=0 center plane, owing to the free surface at the top and also due to the fact that the impeller blades are not perfectly centered with respect to the impeller disc. The effect can be seen as a slight asymmetry that persists even in the mean flow. However, the degree of asymmetry is not severe, so for simplicity the computations assume an approximate symmetry in the neighborhood of the impeller. The presence of tip vortices can be observed both in phase-averaged and instantaneous vector plots. The phase-averaged velocities also suggest the presence of a jet with a dominant radial component; this is evident from the vector fields at θ=0° and 50°, where a strong radial flow can be seen in spite of almost no discernible core of tip vortices. The flow is quite unsteady with the jet induced by the impeller and the tip vortices meandering up and down the center plane (z=0); the time-dependence is more clear when all the 100 realizations are viewed and compared with the phase-average. In all these figures the projected view of the impeller blade is also shown. Light reflected from the blade tip adversely affects the velocity measurement in a small region close to the bottom tip at θ=0° (Sharp *et al.* 1999).

Figure 2 also shows the stereoscopic PIV measurement system for the θ-z surface measurement. The measurement on the curved surface is achieved by first obtaining data on three x-z planes. The trigger delay is adjusted such that the blades are in position as shown in figure 2 at the time of data acquisition. More details on the stereoscopic PIV measurement are given in Hill *et al.* (2000). Experimental results are obtained for three different rotation rates of 50, 100 and 150 rpm corresponding to mixing Reynolds numbers of approximately 2000, 4000 and 6000, which are in the transitional regime. Sample instantaneous velocity fields at the three measurement planes are shown in figure 5. One hundred such instantaneous velocity fields are accumulated and averaged at each location, and the resulting data are

interpolated onto a cylindrical surface that is enclosed by the data planes. Figure 6a shows the averaged axial-circumferential velocity field on the cylindrical surface for 100 rpm. This data is obtained by averaging an ensemble of 100 stereo PIV realizations plotted as a function of z and θ. Only a 60-degree sector between two adjacent blades of the Rushton turbine is shown. The data is also symmetrized about z=0 and hence only the top half of the swept surface is shown with the bottom half below the impeller disk being the mirror image of the top half. The radial location of the cylindrical surface is at R=26mm. The corresponding contours of the out-of-plane radial velocity on this cylindrical surface are shown in figure 6b. As shown in figure 1 this cylindrical surface cuts through the tip vortex pair and the imprint of the tip vortex pair can be seen in figure 6a as the crowding of the vector field around θ=12° and z=0. A corresponding increase in the radial velocity can also be observed due to the influence of the tip vortex pair. The flow field in figure 6a is dominantly in the negative θ direction, arising from the impeller induced circumferential flow (note that the blade is also rotating in the negative θ direction).

3. Theoretical Model of Impeller-induced Flow

As schematically shown in figure 1, the dominant effect of the rotating Rushton impeller is to generate a mean circumferential flow, a jet flow and pairs of blade tip vortices. In the case of a Rushton turbine the jet flow slowly changes direction from a circumferential direction to a more radial direction with increasing distance from the axis of the impeller. Furthermore, the tip vortex pair is on average nearly symmetric. Here we will consider in detail simple theoretical models of these individual components and how the experimental measurement fits the theoretical model.

3.1 Tangential Jet

The jet flow from a Rushton turbine is traditionally approximated as a radial jet (Schwarz 1963). Under boundary layer assumptions a fully consistent analytic self-similar solution can be obtained for the radial jet. However, experimental results suggest that the data can be better approximated when the impeller-induced flow is modeled as a tangential jet (Nielsen 1958). Using the results of Nielsen (1958), Desouza & Pike (1972) separated the stirred tank into several regions and used different theoretical models to describe the flow in each region. A tangential jet model was used to describe the flow in the impeller region and two-dimensional potential flow and jet models were used to describe the flow over the rest of the tank.

The tangential jet is purely circumferential at its virtual source but progressively turns to a radial orientation as radius increases out from the virtual source, due to centrifugal effects (Nielsen 1958,

Desouza & Pike 1972). This flow can be thought of as resulting from an infinitely thin circular ring of radius a, rotating infinitely fast in an unbounded fluid medium, but imparting finite net momentum to the fluid. Standard boundary layer theory can be applied and an approximate self-similar solution can be obtained. In this model the jet has three components of velocity, but they depend only on the radial and axial coordinates. The jet velocity can be expressed as

$$u_{Jq} = U_J\left\{1-\tanh^2(\eta)\right\}, \tag{1}$$

where the centerline velocity of the jet, U_J, shows the following behavior with the radial location, r:

$$U_J = \frac{A}{r^{1/2}}\frac{1}{\left(r^2-a^2\right)^{1/4}} \tag{2}$$

and the self-similar axial distance, η, is defined as

$$\eta = \frac{\sigma z}{\sqrt{r^2-a^2}}. \tag{3}$$

From the above jet velocity the radial and circumferential components of the jet can be obtained in terms of the jet angle, $\theta_J = \cos^{-1}\left[\sqrt{r^2-a^2}\,/\,r\right]$, as

$$u_{Jr} = u_{Jq}\cos(\theta_J) \quad \text{and} \quad u_{J\theta} = u_{Jq}\sin(\theta_J). \tag{4}$$

In the above equations A measures the momentum of the jet and σ measures the width of the jet (jet thickness parameter). At the virtual origin ($r = a$) the jet is entirely circumferential, and for $r >> a$ the jet is entirely radial. Owing to entrainment there is an axial component to the circular jet, which can be obtained from the continuity equation as

$$u_{Jz} = U_J\left\{\frac{z}{\left(r^2-a^2\right)^{1/2}}\left[1-\tanh^2(\eta)\right]-\frac{(2r^2+a^2)}{2\sigma r^2}\tanh(\eta)\right\}. \tag{5}$$

The above solution is an approximate self-similar solution to the boundary layer equations, and it becomes exact as $r >> a$. Eqns. (1) to (5) exactly conserve jet momentum

$$2\pi r\int_{-\infty}^{\infty} u_{Jq}^2\,dz = \frac{2\pi r^3}{\left(r^2-a^2\right)}\int_{-\infty}^{\infty} u_{Jr}^2\,dz = \text{constant}. \tag{6}$$

In this model the three parameters that control the jet flow are: the virtual origin (a), the jet strength (A) and the jet width (σ). Later we will extract the value of these three parameters from experimental data. It must be pointed out that other approximations to the impeller-induced jet flow are possible. One such approximation is the turbulent swirling radial-jet model (Kolar *et al.* 1982, 1984 and Kresta & Wood

1991), which has some advantages over the tangential jet model. Nevertheless, here we will pursue the tangential jet model, mainly for its simplicity. As will be shown below, the tangential jet model provides an adequate description of the impeller-induced flow for the present purposes.

The velocity field shown in figure 6 around the impeller swept volume includes contributions from both the jet and the tip vortex pair. To obtain the parameters associated with the jet from the experimental measurement it is necessary to isolate the contribution of the jet. While the jet component is taken to be independent of the azimuthal direction (θ), the velocity contribution from the tip vortices is strongly dependent on θ. At the surface of the impeller swept volume shown in figure 6 the center of the tip vortex pair is located at about 12° to the blade location (this assertion will be verified below). For large distances, the influence of the tip vortex decays as inverse distance from the vortex core. Thus, as we move away to $\theta \approx 45°$, the velocity field is likely to be dominated by the jet component. Furthermore, on the θ-z plane of the impeller swept volume, where the experimental measurements are taken, the radial component of velocity is dominantly due to the jet;and the contribution from the tip vortices and circumferential flow are likely to be minimal. Based on above arguments the experimental radial component of velocity in the region $\theta = 40°$ to 50° is dominated by the jet flow and little influenced by the tip vortices. The circumferential, radial and axial velocities obtained from the stereoscopic PIV measurements are shown in figure 7 at three different circumferential locations (θ=40°, 45° and 50°). The circumferential and radial components show little variation confirming that the nearly uniform flow in this region is dominantly due to the jet. Owing to its smaller magnitude some variation can be seen in the axial component of velocity, possibly due to the influence of flow around the impeller located at θ=60°. The jet parameters, a, A and σ, are determined using a nonlinear optimization procedure by projecting the stereoscopic PIV data in the region $\theta = 40°$ to 50° onto the theoretical model given in Eqns. (1) to (5). The resulting optimal jet parameters in nondimensional terms are: a=0.67, A=0.163 and σ=5.0. Figure 7 also shows the model velocities obtained from Eqns (1) to (5) using the above values. The model represents the radial and axial components well.

A constant lag can be seen in the case of circumferential velocity, which was also observed by Desouza & Pike (1972). Here we associate the difference to a circumferential flow, $u_{C\theta}(r)$, which is considered to be axisymmetric and independent of the axial direction. $u_{C\theta}$ can be considered as an average swirling flow in the tangential direction that exists in addition to the tangential jet. Figure 7 shows that a circumferential flow defined in nondimensional terms as $u_{C\theta}$ =-0.42 is able to reproduce the experimental

measurement accurately. Thus the circumferential flow component has also been determined from the PIV measurement.

3.2 Tip vortices

The tip vortices are generated from the roll-up of the shear layers as flow accelerates around the rotating impellers. Their presence has been suggested by past experimental observations and measurements (van't Riet & Smith 1975, Yianneskis, Popiolek & Whitelaw 1987 and Calabrese & Stoots 1989). Here we follow a modified version of the procedure introduced by Placek & Tavlarides (1985) for the tip vortex model. As shown in figure 1, the trajectory of each tip vortex pair is curved. The tip vortices are characterized by their trajectory (their radial and axial position), their strength, $\Gamma(\theta)$, and size, $\delta(\theta)$, where again θ measures the angle from the impeller blade in the direction opposite to the blade rotation. First we extract the trajectory of the vortex from the PIV measurements in the r-z and θ-z planes. Measurements of the mean velocity field in the r-z plane at θ=10°, 20°, 30°, 40° and 50°, after subtraction of the jet and circumferential flow components, are shown in figure 8. The data have been symmetrized about z=0, and only the top half above the impeller plane is shown. The presence of a pair of vortices can be clearly seen after the jet contribution has been removed. With increasing θ the vortex centers can be observed to move out in r and the axial separation of the vortex pair also slightly increases. Figure 9a shows the trajectory of the vortex in the x-z plane and the circle traced by the tip of the impeller. The corresponding trajectory in the z-θ plane is shown in figure 9b. A simple linear fit through the data as follows

$$r_v(\theta) = 0.86 + 0.47\theta \qquad \text{and} \qquad z_{v\pm}(\theta) = \pm\left(0.06 + 0.08\theta\right) \tag{7}$$

provides an adequate description of the radial and axial location of the center of the tip vortex pair (z_{v+} and z_{v-} corresponds to the vortex above and below the center plane at z=0).

For the velocity boundary condition it is of interest to obtain all three components of velocity induced by the tip vortex system at any point **P** along the impeller swept boundary. With a description of the vortex trajectory and strength, the velocity induced at any point **P** can be expressed as a line integral according to the Biot-Savart law (Saffman 1992). Considerable simplification can be achieved by assuming that the dominant influence comes from a point **Q** along the vortex where the vortex axis is normal to the line joining **P** and **Q** (see figure 10). Although this is quite a simplification, the alternative is very complex. So, for every point **P** a companion point **Q** along the vortex pair can be identified whose position is given by

$\left(r_v(\theta_Q), \theta_Q, z_{v\pm}(\theta_Q)\right)$. The tip vortices are assumed to be viscous and velocity induced at point $\mathbf{P}$ is then given by

$$u_{Vs} = -\frac{\Gamma}{2\pi}\left[\frac{z_+}{d_+^2}\left\{1-\exp\left(-\frac{d_+^2}{\delta^2}\right)\right\} - \frac{z_-}{d_-^2}\left\{1-\exp\left(-\frac{d_-^2}{\delta^2}\right)\right\}\right] \tag{8a}$$

$$u_{Vz} = -\frac{\Gamma}{2\pi}\left[\frac{r_s}{d_+^2}\left\{1-\exp\left(-\frac{d_+^2}{\delta^2}\right)\right\} - \frac{r_s}{d_-^2}\left\{1-\exp\left(-\frac{d_-^2}{\delta^2}\right)\right\}\right] \tag{8b}$$

where r_s measures distance between $\mathbf{P}$ and $\mathbf{Q}$ along a plane perpendicular to the tank axis and normal to the vortex trajectory (see figure 10). $z_\pm$ measures axial distance from the top and bottom tip vortices and $d_\pm$ measures the total distance from the top and bottom tip vortices. Here Γ and δ measure the strength (circulation) and size of the vortices at $\mathbf{Q}$. In Eqn. (8a) u_{Vs} is the vortex induced velocity component along the s axis (line joining the projections of $\mathbf{P}$ and $\mathbf{Q}$ on the z=0 plane; see figure 10), from which the radial, u_{Vr}, and circumferential, $u_{V\theta}$, components can be easily evaluated. Of course, the total influence of all the tip vortices can be evaluated, if needed, by an integration along the vortex trajectory and appropriate summation over all the tip vortex pairs.

The two-dimensional velocity fields measured on r-z planes, after subtraction of the jet component ($\tilde{u}_{Vr}$ and $\tilde{u}_{Vz}$) shown in figure 8, are used to compute the vortex strength and size by comparing them with the above theoretical model. In each plane, attention is focused on the region close to the tip vortices. The amplitude of error between the experimentally measured velocity field and that obtained from the above theoretical model is defined as

$$e(r,z) = \left[\left(u_{Vr} - \tilde{u}_{Vr}\right)^2 + \left(u_{Vz} - \tilde{u}_{Vz}\right)^2\right]^{1/2}. \tag{9}$$

The optimal value of local Γ and δ are evaluated by minimizing the rms error integrated over a region around the vortex. The variation in Γ and δ measured at $\theta = 10°$ to $50°$ is shown in figure 11. A smooth reduction in the vortex strength along its length from its peak value can be observed. The corresponding vortex core size also decreases, possibly due to stretching and possibly due to the fact that the scatter in the instantaneous location of the vortex center increases as the vortex pair moves away from the blade into the tank. Also marked in the figures (as filled circle) are the average values of Γ and δ obtained from a similar error minimization procedure for the stereoscopic PIV measurements on the z-θ plane. For this case we have assumed a constant strength and size for the tip vortex pair along its length in the theoretical

model. Thus the result of the optimization must be interpreted to be an average Γ and δ, averaged over the entire length of the vortex pair. Since the vortex pair cuts this z-θ plane around θ=12°, a larger weighting for small θ and smaller weighting for larger θ is expected in the average. The resulting $\Gamma_{avg} = 0.26$ and $\delta_{avg} = 0.072$, are well within their range measured on individual θ-planes, and as expected the weighted average is close to values obtained at $\theta = 10°$. The measured vortex circulation is the strongest at $\theta = 10°$ with $\Gamma = 0.3$ and is very compact with $\delta = 0.088$, which yields a peak nondimensional vortex induced velocity of $0.1\Gamma / \delta$ for a single vortex, which is about 35% of the blade tip velocity. At $\theta = 50°$ the vortex circulation has fallen to $\Gamma = 0.065$ and its size has changed to $\delta = 0.057$; the corresponding peak induced velocity is now only 11% of blade tip velocity.

3.3 Comparison with experiments

The above analytical expressions for the jet and tip vortex flows are valid only in the region close to the impellers; as we move outward the effect of the outer walls of the tank must be accounted for. Nevertheless, the near-field of the impeller-induced flow can be expressed as

$$\mathbf{u}_I(r,\theta,z,t) = \mathbf{u}_J(r,z) + \mathbf{u}_V(r,\theta,z,t) + \mathbf{u}_C(r) \qquad (10)$$

where $\mathbf{u}_C$ is the mean circumferential flow. It is important to note that, unlike most previous attempts at modeling the velocity boundary conditions, the above model includes all three (radial, circumferential and axial) components of velocity. The impeller induced flow varies along the circumferential direction as well due to the presence of tip vortices. Significantly, inclusion of the tip vortices leads to a time-dependent impeller induced flow (in the laboratory frame of reference) arising from the rotation of the blades.

The above theoretical model needs to be evaluated by comparing the results with experimental measurements. Comparisons will be made in both the r-z and θ–z planes. First, in figure 12, radial velocity profile as a function of axial location at r=1 obtained from the analytical model (Eqn. 10) is compared with the experimental measurements at four different azimuthal locations. The model provides a good description of the experimental measurement. The velocity field on the curved surface surrounding the impeller evaluated from the theoretical model is shown in figure 13. Both the in-plane velocity vector plot (figure 13a) and the out-of-plane velocity contours (figure 13b) compare favorably with the corresponding experimental measurements shown in figures 6a and 6b. A closer comparison of the tip vortex field is shown in figure 14 where the velocity field after subtraction of the jet component is shown for both the

experimental measurement and the theoretical model. The strength of the theoretical model is clear from the favorable qualitative and quantitative comparison.

It can be argued that good comparison between the experiments and the model is to be expected. After all, the parameters for the model were obtained from the experiments. Nevertheless, the experimental data that is being approximated is complex and fully three-dimensional. All three components of velocity are significant, and they vary in all three coordinate directions. A simple curve fit through the experimental data as input for the computations would not satisfy kinematic constraints and could be futile. A sound theoretically based model is essential to capture the complex variation exhibited by the flow. Furthermore, the model reduces the prescription of the boundary condition to a few physically meaningful parameters such as amplitudes and width of the jet and the tip vortices. This allows physically meaningful scaling of the impeller-induced flow with impeller size and speed of rotation. The data for 50, 100 and 150 rpm (i.e., Re=2000, 4000 and 6000) can be used to establish the scaling of the three different impeller-induced flow components. Figure 15 shows variation in circumferential flow, jet strength (A) and circulation of the tip vortex pair (Γ) with Re (all quantities are plotted as a ratio with respected to their value at the intermediate Reynolds number of 4000). It appears that the strength of all three components scale similarly from 2000 to 4000, but differently as Reynolds number increases above 4000. Admittedly, the range of Reynolds number considered is very limited; nevertheless it appears that the three different components are likely to scale differently with increasing Re. This provides a possible explanation for the complex scaling for the overall impeller-induced flow that is often observed in the laboratory studies.

The theoretical model presented above is by no means perfect. Improved models of the jet flow and tip-vortices can be sought. For example, the tangential jet model could be replaced by a swirling radial-jet model (Kolar *et al.* 1982, 1984 and Kresta & Wood 1991). More importantly, instantaneous PIV realizations clearly reveal that the individual flow components are time dependent. For instance, the impeller-induced jet appears to oscillate up and down about its mean radial trajectory, resulting in a faster axial spreading of the jet flow. Such asymmetry seems to exist between the top and bottom tip vortices as well at any given instance in time. The theoretical framework can be extended to introduce the effect of asymmetry in a controllable manner; for example, both the amplitude and frequency of asymmetry can be controlled.

4. Computational Approach

We have performed Reynolds averaged Navier-Stokes simulations of flow inside the stirred tank at Re=4000 using the commercial code FLUENT®. The impeller-induced flow on the surface of the swept volume is used as the input driving mechanism for the flow. The computations are performed in a frame of reference rotating with the impeller. In this rotating frame, the model for the impeller-induced velocity field, c.f. figure 13, appears as a steady boundary condition. In the absence of any baffles the statistics are stationary, independent of time, in the rotating frame of reference. Thus a Reynolds averaged simulation for the time-averaged flow is appropriate. The time-averaged flow has a six fold symmetry and here we consider only a 60° sector between adjacent impeller blades and simulate the flow inside this region with periodic boundary conditions to extend the flow over the entire 360°.

The velocity field shown in figure 13, appropriately adjusted for the rotating frame of reference, is applied as the boundary condition at the surface of the impeller swept volume (r=1). The no-slip boundary conditions at the bottom and the outer tank surfaces transform in the rotating frame of reference to surfaces rotating in the opposite direction. For simplicity the top surface is also considered to be no-slip. Simulations performed with stress-free boundary condition at the top do not differ substantially. A symmetry boundary condition is used at r=0. The details of the overall computational geometry in the r-z plane and the boundary conditions are shown in figure 16.

An important consequence of including the tip vortices in the theoretical model is that the boundary condition is dependent on the azimuthal direction. The jet and the circumferential flow are independent of θ. Thus even in the context of Reynolds averaged simulation for the time-averaged flow, a three-dimensional simulation within the 60° sector is required. A three-dimensional grid of 40×81×16 points along the radial, azimuthal and axial direction is used to compute the flow. A non-uniform grid with grid clustering near the impeller region is used in all three directions in order to better resolve the complex flow near the impeller (see figure 17 for the grid distribution). For comparison a simultaneous two-dimensional Reynolds averaged simulation is also performed, where the flow is assumed to be independent of the θ–direction. In the two-dimensional simulation, the velocity field shown in figure 13 is θ-averaged and applied as the boundary condition for the impeller-induced flow. The geometry and other boundary conditions on the r-z plane are the same as in the three-dimensional simulation.

Figures 18a and 18b show the velocity vector plot on the r-z plane computed from the three-dimensional and the two-dimensional simulations. Both the flows appear to be qualitatively similar with a

pair of large vortices that span the entire top and bottom halves of the stirred tank. However a number of subtle differences can be observed. The centers of the large eddies are located at a radial position of $r\approx2.2$. In the case of the two-dimensional simulation the center's axial position is farther away from the centerline at $z\approx\pm0.8$, whereas in the three-dimensional simulation the centers are somewhat closer to the centerline at $z\approx\pm0.6$. Also, in the case of three-dimensional simulation the impeller-induced jet after hitting the outer wall turns and travels all the way to the top and the bottom of the tank before returning back to the impeller; thus the pair of eddies cover almost the entire tank. In the case of the two-dimensional simulation the eddies separate from the outer wall before reaching the top and the bottom. As a result, they generate a pair of secondary eddies located in the outer top and bottom corners of the tank, whose direction of rotation is opposite to those of the primary eddies. This difference might have a strong influence on the degree and extent of mixing predicted by the two different simulations.

The width of the impeller-induced jet-like flow increases rapidly from its starting point at $r=1$ in the case of the two-dimensional simulation, whereas in the case of three-dimensional simulation the jet stays focused for a short radial distance (up to about $r\approx1.25$) before spreading. This difference can be seen clearly in the centerline ($z=0$) radial velocity profile for both the two- and three-dimensional simulations (figure 19a). The three-dimensional results are averaged along the θ-direction. Also plotted for comparison are the corresponding experimental θ-averaged measurement. In both the three-dimensional simulation and in the experimental measurements the azimuthal-averaged radial velocity can be seen to first increase with r before decaying like a jet. This increase is due to the influence of tip-vortices, whose sense of rotation is such that they increase the radial component of velocity. The tip-vortices' influence is confined to their neighborhood, thus resulting in an increase in radial velocity immediately following the tip radius ($r=1$). Farther away the influence of the jet dominates, resulting in the decay of the radial velocity. The predicted maximum radial velocity lies farther out from the tip than the experimental maximum as previously been observed in time-dependent three-dimensional large-eddy simulations (Eggles 1996 and Revstedt *et al.* 1998). On the other hand, most Reynolds averaged simulations have failed to accurately capture the presence of the tip vortices and without their influence the radial velocity decays monotonically immediately from its maximum value at the blade tip. Note that with the improved boundary condition, which incorporates the effect of the tip vortex pair, even Reynolds-averaged simulation is able to capture the effect of tip vortices in the interior. Figure 19 also shows the computational results of Revstedt *et al.* (1998). Their geometry and operating conditions are somewhat different, and in order to facilitate comparison their result has been scaled to match the velocity at $r=1$. Very good comparison between

Revstedt *et al*'s. (1998) data and the three-dimensional simulation can be seen, but neither agrees very well with the experiments.

The influence of the tip vortices can be more clearly seen in figures 19b, 19c and 19d where u_r is plotted against r at three different azimuthal locations (θ=10°, 20°, and 30°) for the three-dimensional simulation. The corresponding experimental measurements and the θ-independent result of the two-dimensional simulation are also plotted. The influence of the tip-vortices is most dominant around θ=20°. As the strength of the tip vortex pair decays for larger angles, their influence on the radial velocity also diminishes. One significant difference between the three-dimensional simulation and the experimental data is that the experimental result falls off from the peak faster than the simulation. This difference can be traced back to the fact that while the experimental result showed that the jet centerline oscillated about z=0 at the exit of the impeller, the computations with a time-averaged mean boundary condition ignored this oscillation. As a result the mean spreading rate of the jet is faster in the case of the experiment, resulting in a faster drop-off of the centerline velocity. Thus, it appears that a time-dependent boundary condition at the exit of the impeller may be required in order to obtain better comparison with the experimental data. Another difference between the experimental data and the computation is that the peak radial velocity in the case of the experiment falls of faster with increasing θ. While at 10° and 20° the peak radial velocity obtained in the three-dimensional computation compared reasonable with the experimental measurement, at 30° the computational peak is significantly lower than the experimental peak. This is because the strength of the tip vortices is not properly maintained in the Reynolds averaged simulation. As a result, the tip vortex decays faster, and the peak radial velocity induced by the tip vortex pair falls faster. This indicates that a time-dependent simulation, such as large eddy simulation or unsteady Reynolds averaged simulation, with the theoretical model as the boundary condition may be able to perform even better than RANS.

Figure 20 shows the velocity vector plot from the three-dimensional simulation at various azimuthal locations in the region close to the impeller swept volume. The tip vortices can be seen clearly from 0° to about 20°. They persist for θ>20° as well, but they are too weak to be directly identified from the total velocity field. They can be isolated and extracted by subtracting out the jet component. Interestingly the tip vortex can be seen also at θ=0°. In reality, due to the presence of the impeller blade the axis of the tip vortex pair turns sharply and run parallel to the blade as shown schematically in figure 1. In the computation, the presence of the impeller blade is not directly accounted for; only its influence is modeled

as the inlet velocity field. As a result the tip vortex pair can be seen to extend even backwards up to $\theta=0°$ with its radial location correspondingly falling below the tip radius of $r=1$.

Figure 21a shows the in-plane velocity vector on a θ-z plane located at $r=1.1$ obtained from the three-dimensional simulation. The corresponding out-of-plane radial velocity is shown in figure 21b. The vector plots clearly show the presence of tip-vortices extending into the tank in the three-dimensional Reynolds averaged simulation. They have an influence on the radial velocity as well. The radial velocity can be observed to increase since the tip vortices cut the constant r plane at an angle. With increasing radial location the azimuthal and the axial location of the vortex centers change, describing the vortex trajectory as captured by the simulation. A detailed comparison shows that quantitative differences exist between the computational results and the experimental observation. In particular, the tip vortex influence decays more rapidly in case of the Reynolds averaged simulations. A time-dependent simulation which resolves the dynamics of at least the largest scales is necessary in order to recover more physics in the simulation.

5. Conclusion

Two sets of experiments have been performed to quantify flow induced by a six blade Rushton turbine in a stirred tank without baffles. The first set of PIV measurements was taken on six different r-z planes phase locked at 0°, 10°, 20°, 30°, 40° and 50° with respect to the blade location. The second set of measurements employed a novel arrangement such that stereoscopic PIV measurements could be obtained on a curved θ-z plane whose radial location is just outside the impeller blade tip radius.

The experimental measurements are used to construct a velocity boundary condition for numerical simulation. The computation is limited to the region outside the impeller swept volume and the impeller-induced flow is applied as the inlet boundary condition. The impeller-induced flow, as measured in the experiments, is quite complex. It has all three-components of velocity, dependent on all three coordinate directions. In this sense the velocity boundary condition significantly extends earlier attempts wherein the impeller-induced flow was modeled as a jet flow, and the θ-dependence of the flow was typically ignored. It must be emphasized that owing to the complex nature of the three-dimensional impeller-induced flow a curve fit through the experimental data, which might serve as the appropriate computational boundary condition, is not straightforward.

We have taken a physics based approach to describing the impeller-induced flow. Experimental measurements show that the flow in the vicinity of the impeller can be decomposed into a circumferential

flow, a jet flow, and pairs of tip vortices associated with each impeller blade. Simple models for each of these flow components are constructed to produce a overall model for the impeller-induced flow. According to the model, the circumferential flow is characterized by its radial profile and is independent of both θ and z; the jet flow is characterized by its strength, width and virtual origin; and the tip vortices are characterized by the location of their centers, strength and thickness along their backbone. Thus, the model allows for a compact characterization of the complex impeller-induced flow with a small number of parameters. Note that changes in the blade design could be represented by these parameters. For example, impellers with tilted blades can be modeled by tip vortices having unequal strength. Comparison of the theoretical model with the experimental measurements both on the r-z and θ-z planes show that the model provides an adequate description of the impeller-induced flow.

Scaling is a central issue in the design of stirred tank reactors. In particular, scaling of the impeller-induced flow with impeller geometry and operating condition has been very challenging. The theoretical model provides a framework to examine complex scaling of the impeller-induced flow. The scaling of the circumferential flow, jet and tip vortex components of the impeller-induced flow has been obtained over a narrow range of impeller rpm. The result shows that each component might follow a simple scaling law, but the overall impeller-induced flow can exhibit complex scaling, since the scaling of each of the component is different.

The theoretical model presented here is simple and provides ample opportunity for further improvement, whereby additional complex physics associated with the impeller-induced flow can be built into the model. The instantaneous realizations show that the impeller-induced flow, even in the vicinity of the swept volume, is time-dependent. The time-dependence can be introduced into the model in several different ways. Parametrization implicit in the model allows for time dependent strength and width for the different flow components. The amplitude and frequency of time-dependence can be varied to better match the experimental observation. A closer look at the instantaneous PIV measurements on the r-z plane reveals that the nature of the time dependence is such that the centerline of the jet flow out of the impeller is not strictly aligned with the radial direction. The direction of the jet flow appears to oscillate up and down about z=0 plane. It is not possible to ascertain the frequency of such oscillation from present PIV measurements. Furthermore, in the instantaneous realizations the tip vortices which are nominally located above and below z=0 plane (which form a pair) are not perfectly symmetric. Their relative strength appears to vary over time.

Two- and three-dimensional Reynolds averaged Navier-Stokes simulations were performed using the commercial code FLUENT® with the model of the impeller-induced flow as the boundary condition. The three-dimensional simulation included the effect of tip vortices; whereas the θ-average implicit in the two-dimensional simulation eliminates the details of the tip vortices. As a result the three-dimensional results are in better qualitative agreement with the experiments. Even so, the results of Reynolds averaged simulations quantitatively differ from experimental measurement. Dynamics of the different scales of motion needs to be accounted for through a unsteady RANS or direct or large eddy simulation for further improvement in prediction. Nevertheless, the improvement of the present model over the conventional boundary condition is evident in the computational results.

Acknowledgments

HSY, SB and MYH were partly supported by a grant from the Dow Chemical Company. KVS was supported by Mavis Fellowship and National Science Foundation Fellowship. DFH was supported by funding from the Leonard C. and Mary Hoeft Endowed Chair of Engineering.

References

1) Calabrese, R.V. and Stoots, C.M. Flow in the impeller region of a stirred tank, *Chem. Engng. Prog.*, **85**, 43-50 (1989).

2) Desouza, A. and Pike, R.W. Fluid dynamics and flow patterns in stirred tanks with a turbine impeller, *Can. J. Chem. Engng.*, **50**, 15 (1972).

3) Eggels, J.M.G. Direct and large eddy simulation of turbulent fluid flow using the lattice-Boltzmann scheme, *Int. J. Heat Fluid Flow*, **17**, 307-323 (1996).

4) Hill, D.F., Sharp, K.V. and Adrian, R.J. Stereoscopic particle image velocimetry measurements of the flow around a rushton turbine, *Exp. Fluids*, in press (2000).

5) Ju, S.Y., Mulvahill, T.M. and Pike, R.W. Three-dimensional turbulent flow in agitated vessels with a nonisotropic viscosity turbulent model, *Can. J. Chem. Engng.*, **68**, 3 (1990).

6) Kolar, V., Filip, P. and Curev, A.G. The swirling radial jet, *Apl. Sci. Res.*, **39**, 329-335 (1982).

7) Kolar, V., Filip, P. and Curev, A.G. Hydrodynamics of a radially discharging impeller stream in agitated vessels, *Chem. Engng. Comm.*, **27**, 313-326 (1984).

8) Kresta, S.M. and Wood, P.E. Prediction of the three-dimensional turbulent flow in stirred tanks, *AIChE. J.*, **37**, 448-460 (1991).

9) Lee, K.C., Ng, K. and Yianneskis, M. Sliding mesh predictions of the flow around Rushton impeller, *ICHEME Symp. Ser.*, **140**, 47-58 (1996).

10) Luo, J.V., Gosman, A.D., Issa, R.I., Middleton, J.C. and Fitzgerald, M.K. Full flowfield computation of mixing in baffled stirred reactors. In proceedings of the IChemE Research Event, Birmingham, UK., 657-659 (1993).

11) Nielsen, H.J. *PhD Thesis*, Illinois Institute of Technology, Chicago (1958).

12) Pericleous, K.A. and Patel, M.K. The source-sink approach in the modeling of stirred reactors, *PhysioChemical Hydrodynamics*, **9**, 279-297 (1987).

13) Placek, J. and Tavlarides, L.L., Turbulent flow in stirred tanks, I: Turbulent flow in the turbine impeller region, *AIChE J.*, **31**, 1113 (1985).

14) Ranade, V.V., Joshi, J.B. and Marathe, A.G. Flow generated by pitched blade turbines II: Simulation using k-e model, *Chem. Engng. Comm.*, **81**, 225-248 (1989).

15) Rao, M.A. and Brodkey, R.S. Continuous flow stirred tank turbulence parameters in the impeller stream, *Chem. Engng Sci.*, **27**, 137-156 (1972).

16) Revstedt, J., Fuchs, L. and Tragardh, C. Large eddy simulation of the turbulent flow in a stirred reactor, *Chem. Engng. Sci.*, **53**, 4041-4053 (1998).

17) Saffman, P.G. *Vortex dynamics*, Cambridge University Press (1992).

18) Schwarz, W.H. The radial free jet, *Chem. Engng. Sci.*, **18**, 779 (1963).

19) Sharp, K. V., Kim, K. S. and Adrian, R. J. (1998) "A Study of Vorticity and Dissipation Around a Rushton Turbine Using Particle Image Velocimetry," *Proc. 9th Int'l Symp. Applications Lasers to Fluid Mechanics,* Lisbon, July 13-16, pp.14.1.1-10 (1998).

20) Van't Riet, K. and Smith, J.M. The trailing vortex system produced by Rushton turbine agitators, *Chem. Engng. Sci.*, **30**, 1093 (1975).

21) Yianneskis, M., Popiolek, Z. and Whitelaw, J.H. An experimental study of the steady and unsteady flow characteristics of stirred reactors, *J. Fluid Mech.*, **175**, 537 (1987).

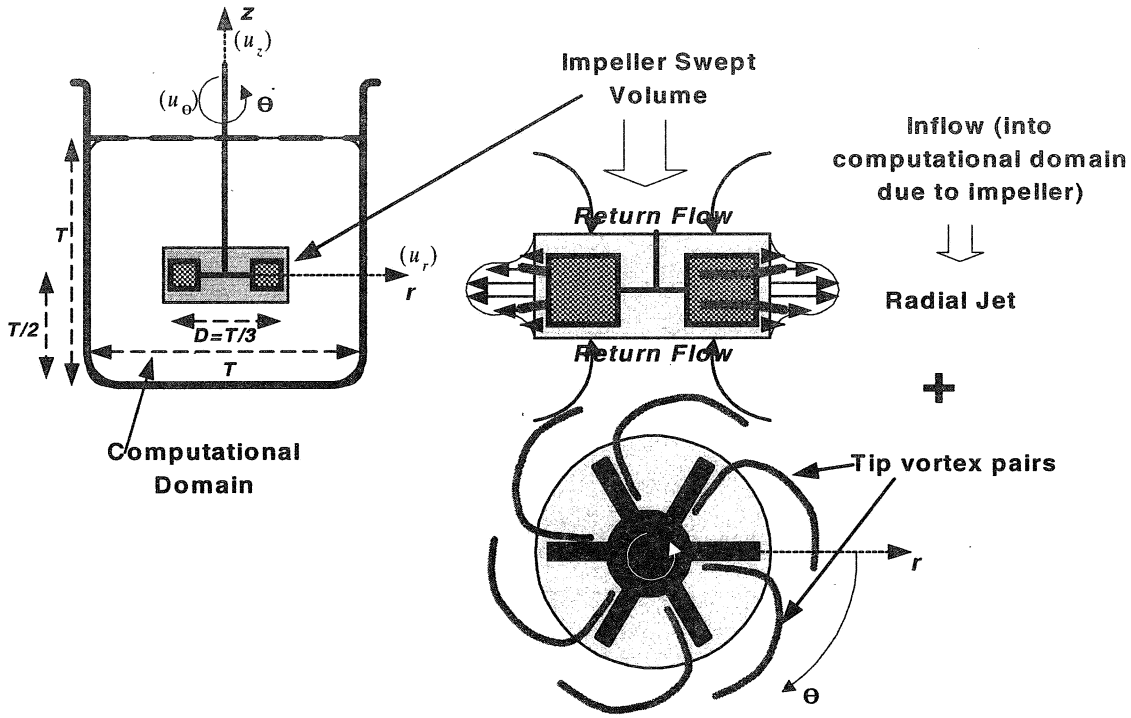

Figure 1. Schematic of the stirred tank with a typical six blade Russian impeller. The plan view shown at the bottom on the right is viewed up from under the tank.

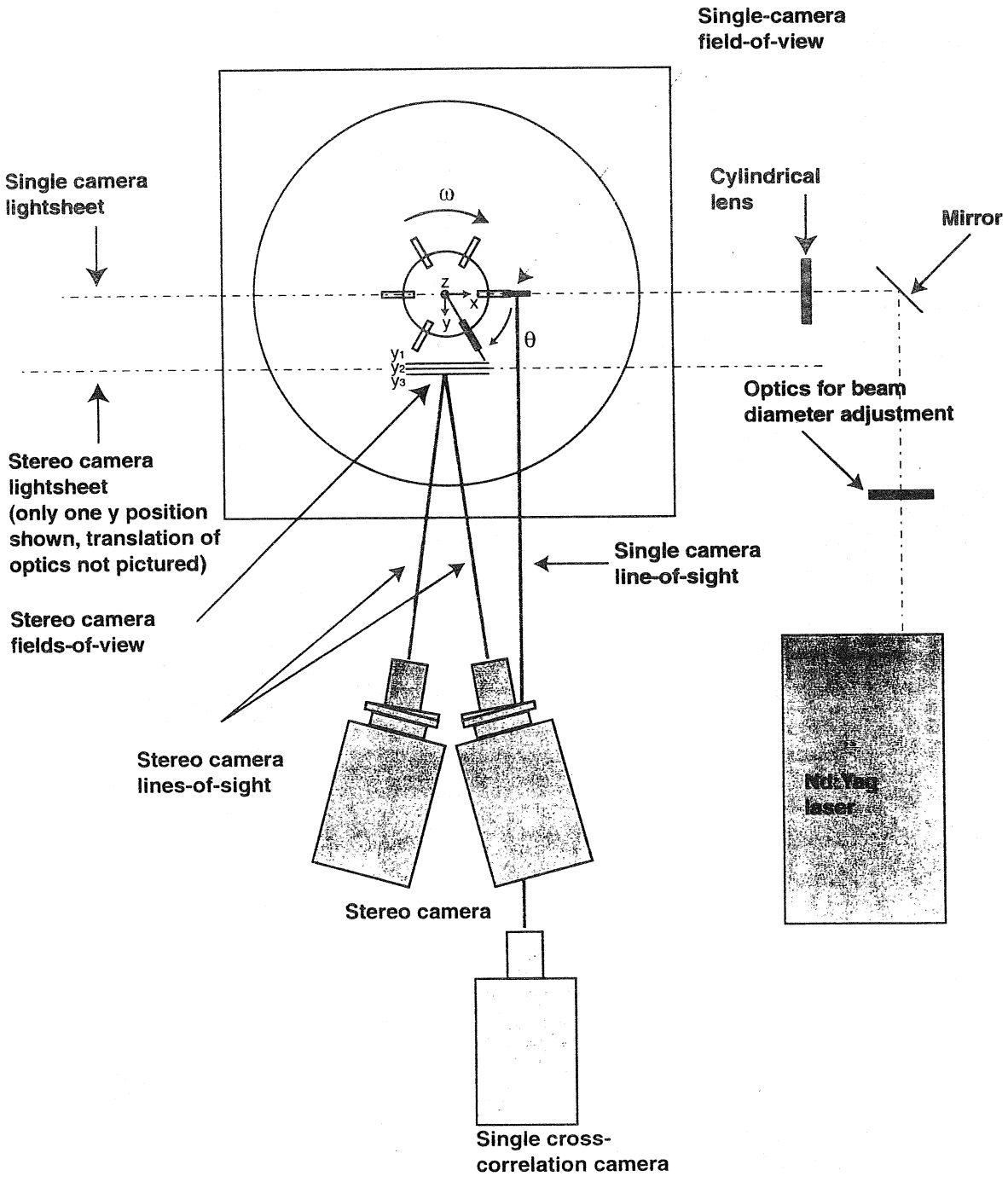

Figure 2: Top view of the experimental apparatus, including tank, blade, laser lightsheet and measurement plane. Arrangement for both the $r-z$ plane and $\theta-z$ surface measurements is shown. The velocity field on the curved surface is evaluated using interpolation of the stereo PIV data obtained on three $x-z$ planes shown in the figure, at distances 22.94, 25.44 and 26.94 mms from the tank centerline.

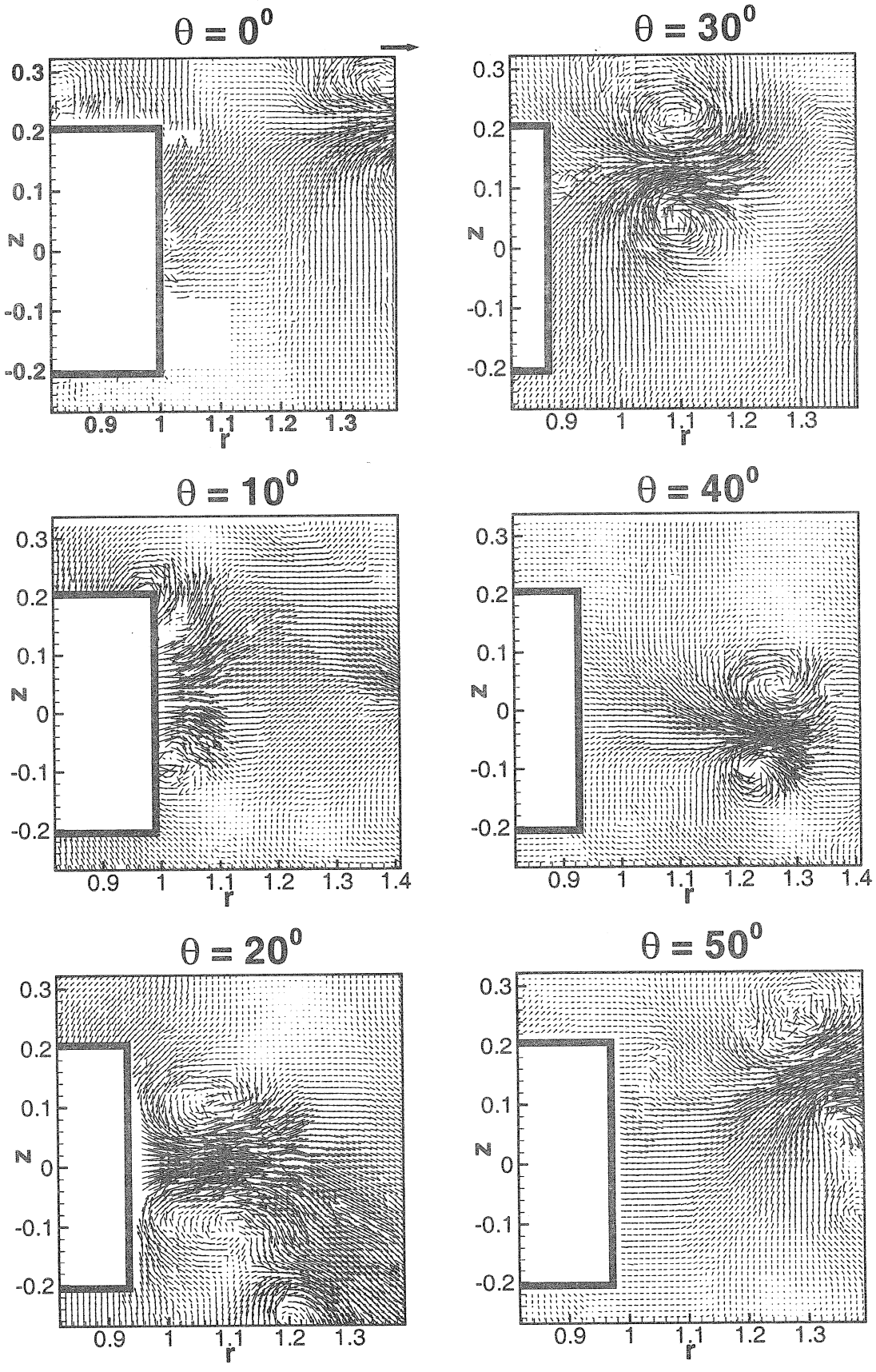

Figure 3: Typical instantaneous velocity fields measured on the $r-z$ planes. (a) $\theta = 0^{\circ}$, (b) 10°, (c) 20°, (d) 30°, (e) 40° and (f) 50°. The reference vector in frame (a) has magnitude of tip velocity.

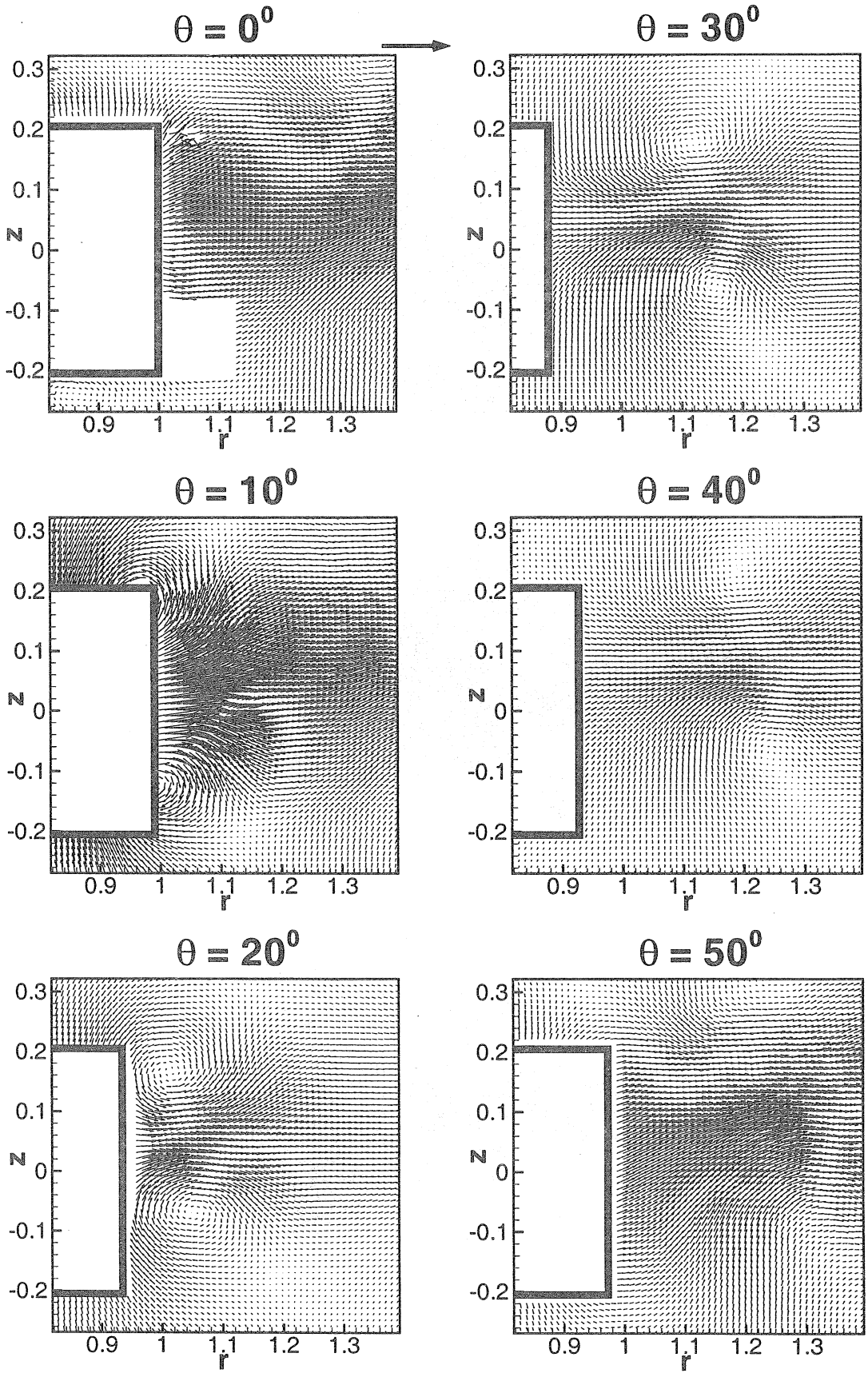

Figure 4: Phase–averaged velocity fields averaged over 100 instantaneous realizations similar to those shown in figure 3. (a) $\theta^{\circ} = 0$, (b) 10°, (c) 20°, (d) 30°, (e) 40°, and (f) 50°. The reference vector in frame (a) has magnitude of tip velocity.

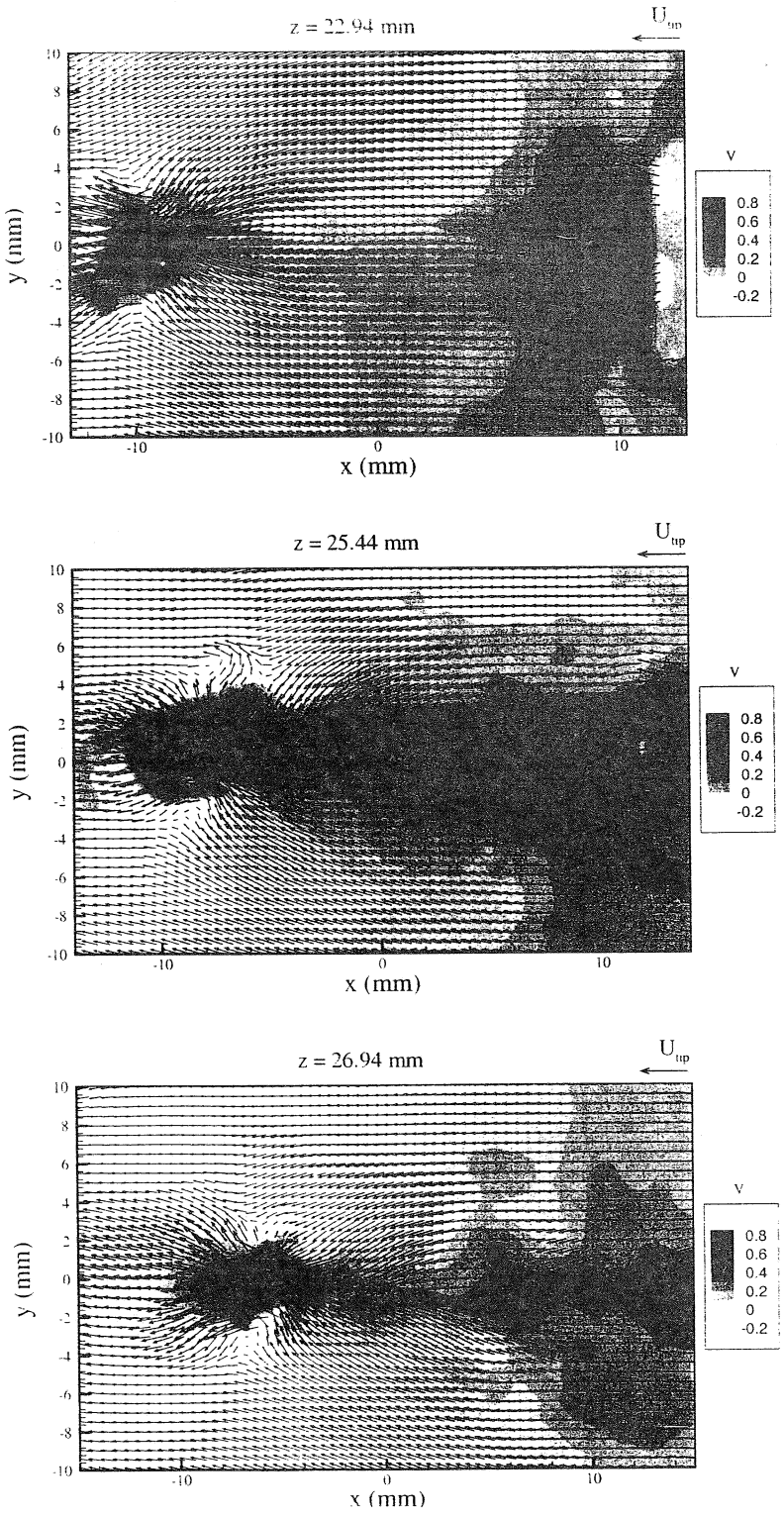

Figure 5: Sample instantaneous three-dimensional velocity field on the three $x-z$ planes for the 100 rpm case. The contours indicate out-of-plane component of velocity. All velocity components have been normalized by the blade tip velocity.

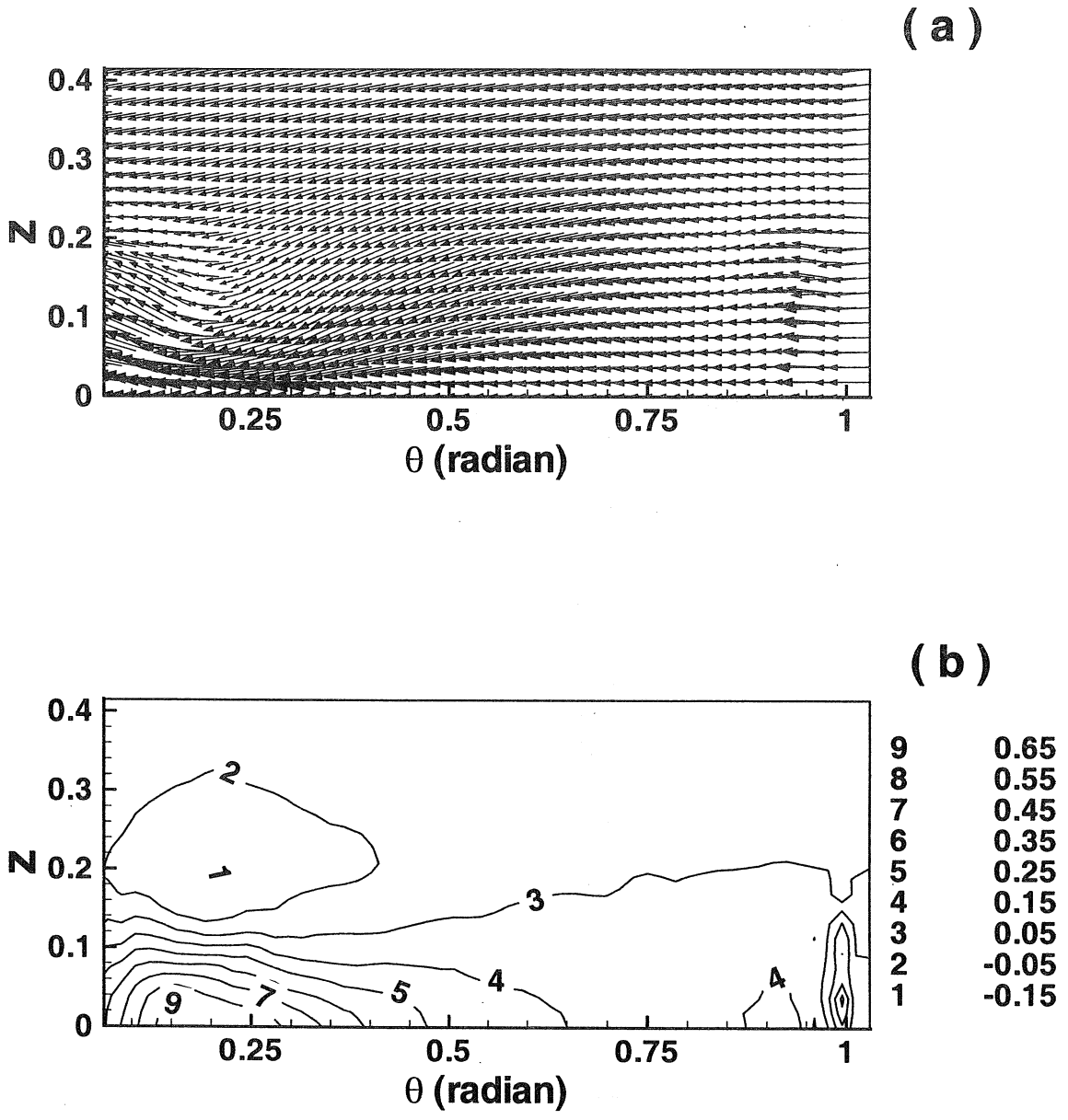

Figure 6: Phase-averaged three-dimensional velocity field on the curved $\theta - z$ surface at $(r \approx 1)$ obtained by averaging over 100 realizations. (a) in-plane velocity vector plot and (b) out-of-plane velocity contour. The disturbance seen on the lower right hand side is due to reflection from the blade.

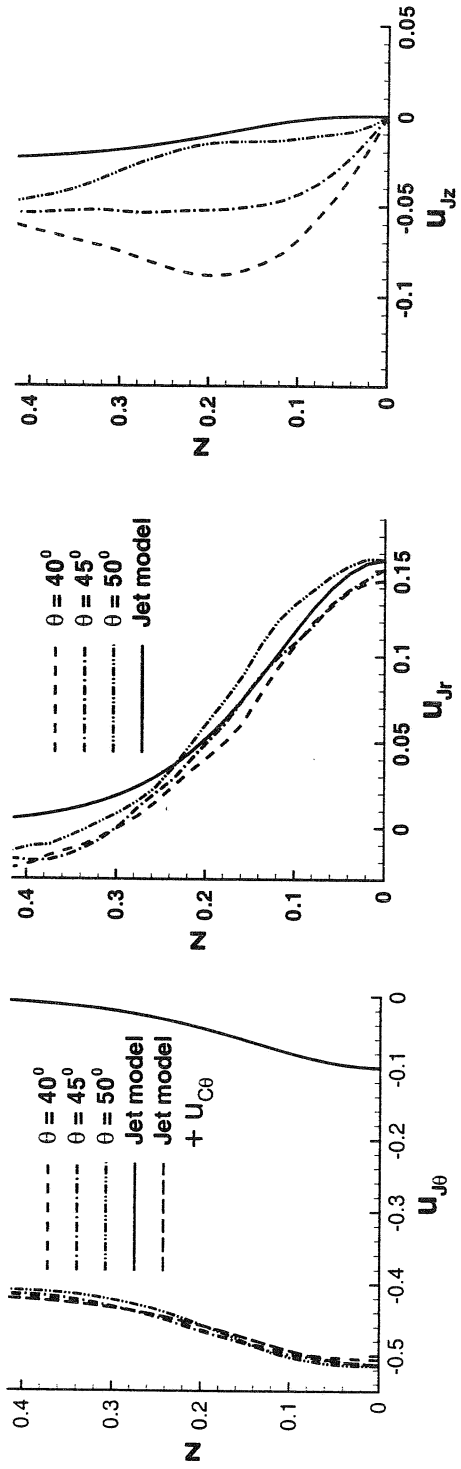

Figure 7: The (a) circumferential, (b) radial and (c) axial velocities obtained from the stereoscopic PIV measurement at three different circumferential locations: $\theta = 40^{\circ}$, 45° and 50°. Also shown for comparison are the corresponding velocity from the theoretical jet model. In the case of u_{θ} profiles with and without the circumferential flow component are shown.

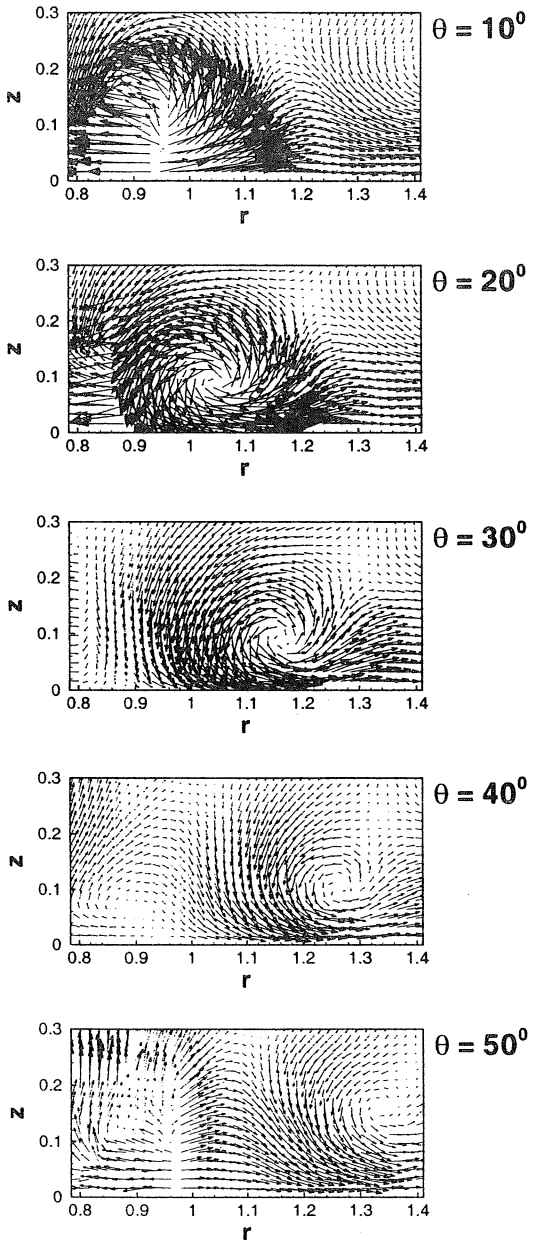

Figure 8: Experimental measurements of mean velocity field in the $r-z$ plane at (a) $\theta = 10^{\circ}$, (b) 20°, (c) 30°, (d) 40° and (e) 50°, after subtraction of the theoretical jet and circumferential flow components.

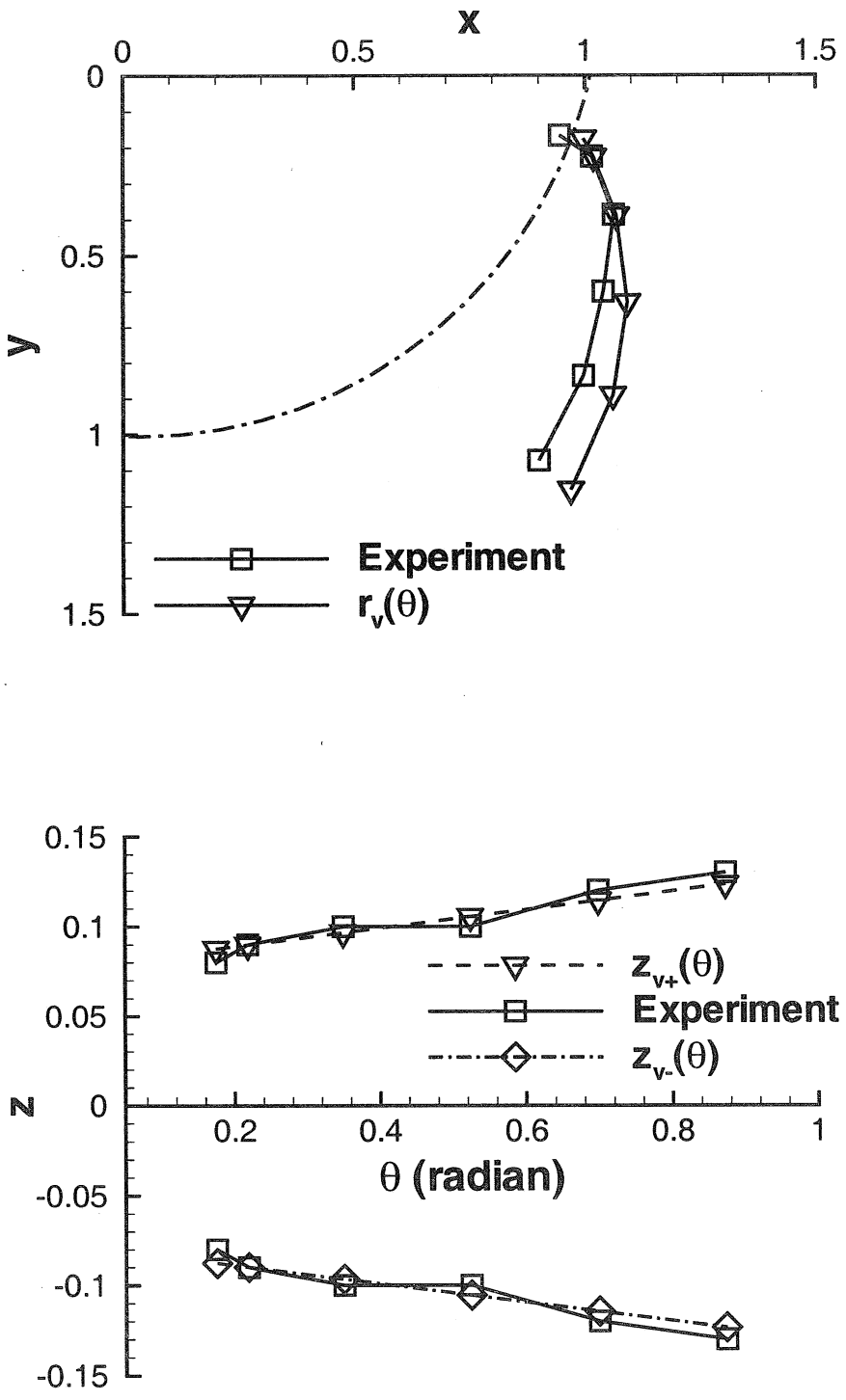

Figure 9: Trajectory of the tip vortex pair in the $x-y$ plane; both experimental measurement and linear fit (Eqn. 7) are shown. Also shown is the circle traced by the blade tip.

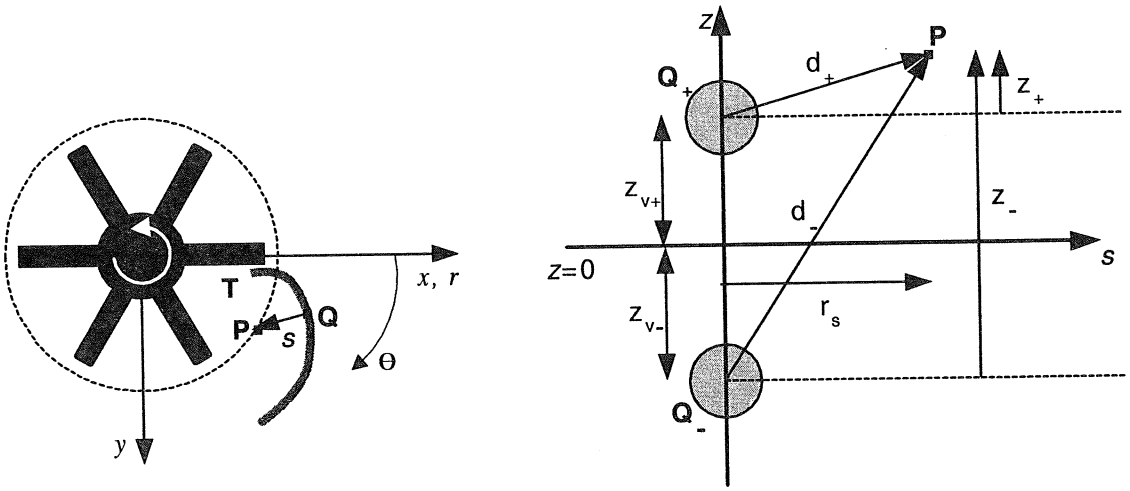

Figure 10: Schematic of the blade tip vortex with respect to the blade position. The direction s is along the line joining $\mathbb{P}$ and $\mathbb{Q}$. Tip vortex pair indicated by $\mathbb{Q}_+$ and $\mathbb{Q}_-$ influence the velocity at $\mathbb{P}$. The plan view shown on the left is viewed up from the bottom of the tank.

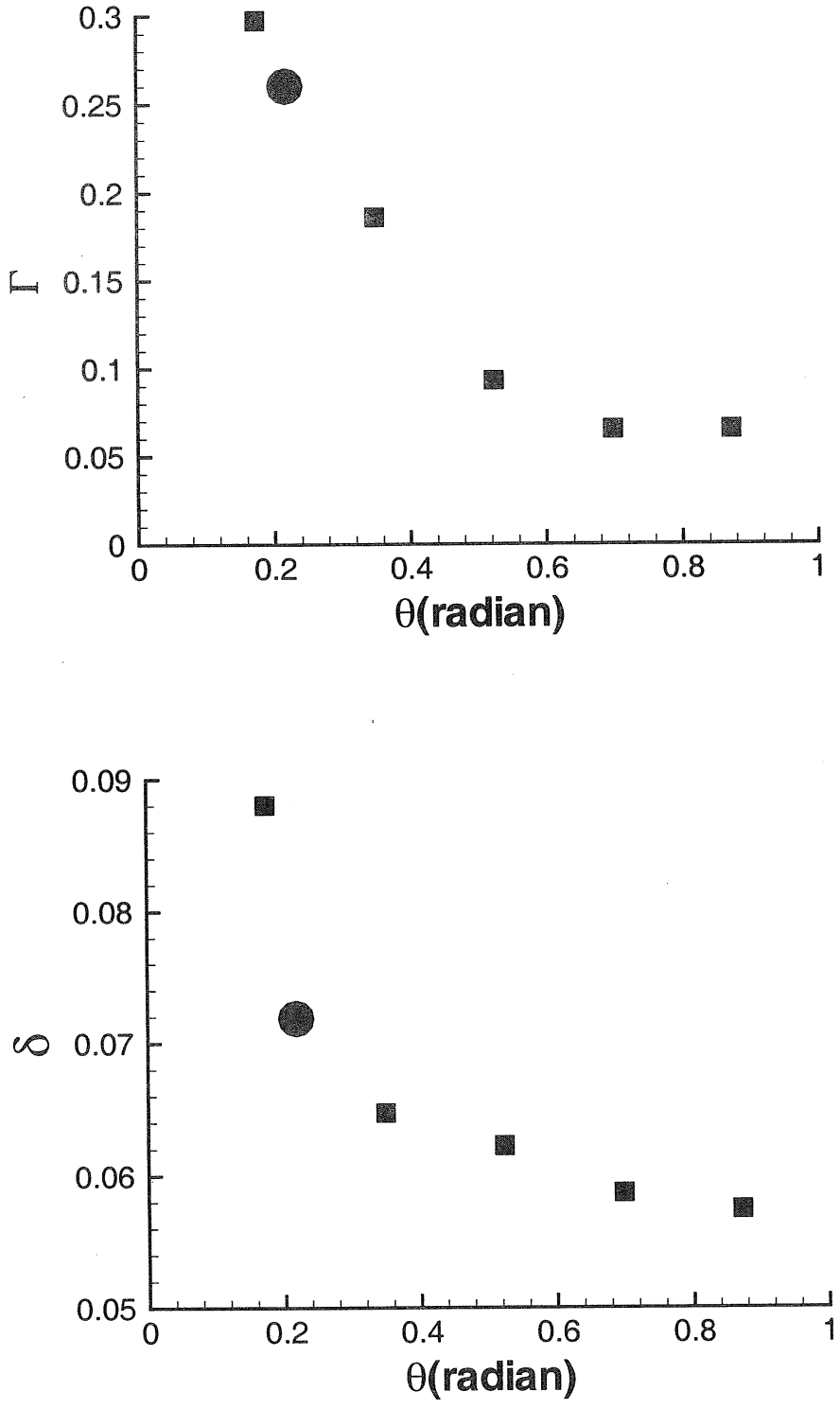

Figure 11: Variation in tip vortex (a) strength and (b) size with θ. ■: obtained from the $r-z$ plane measurements; ●: obtained from the $\theta-z$ surface measurement.

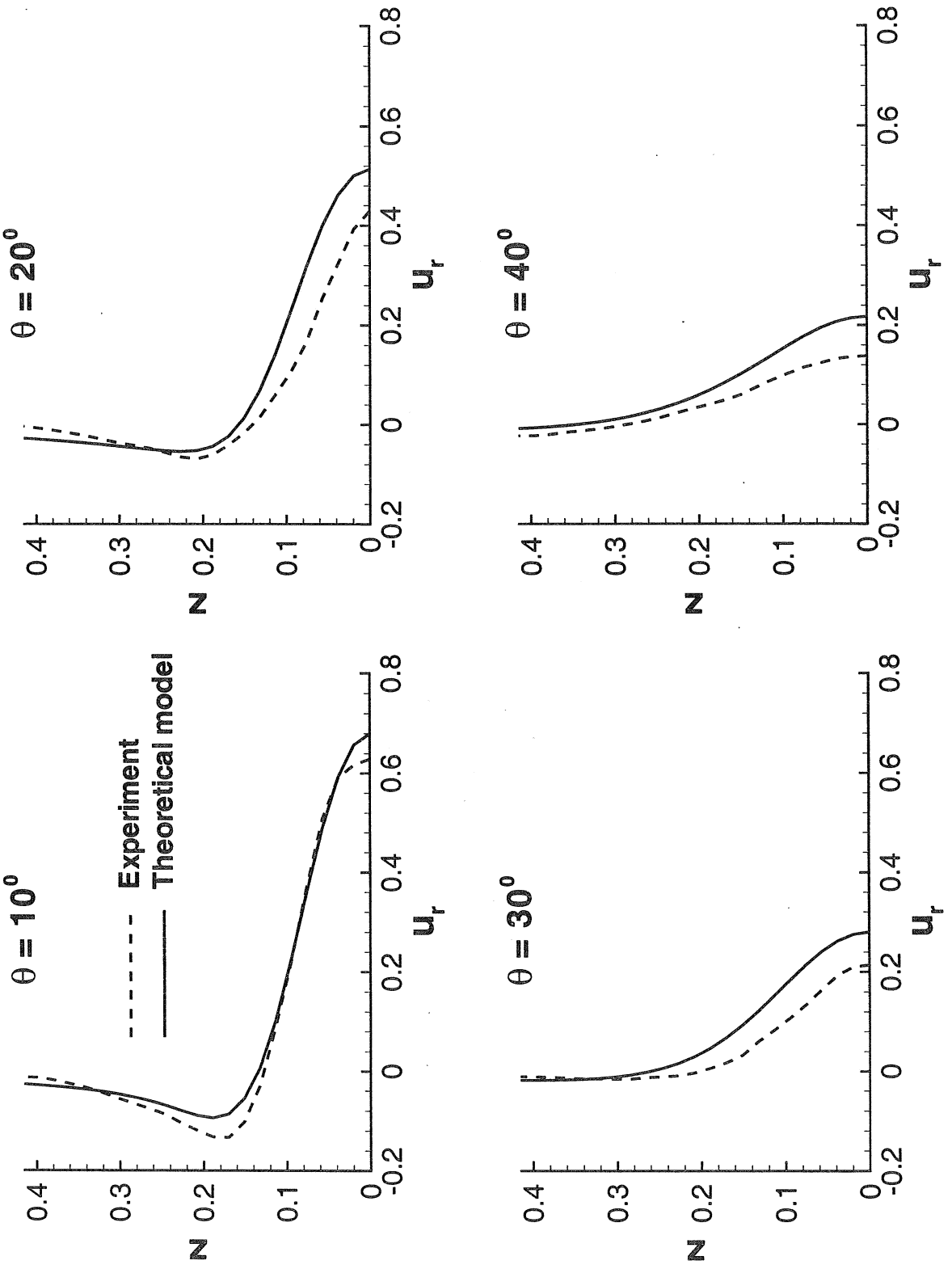

Figure 12: Radial velocity profile as a function of axial location at $r = 1$ obtained from the theoretical model compared with the corresponding experimental measurements. (a) $\theta = 10°$, (b) 20°, (c) 30° and (d) 40°.

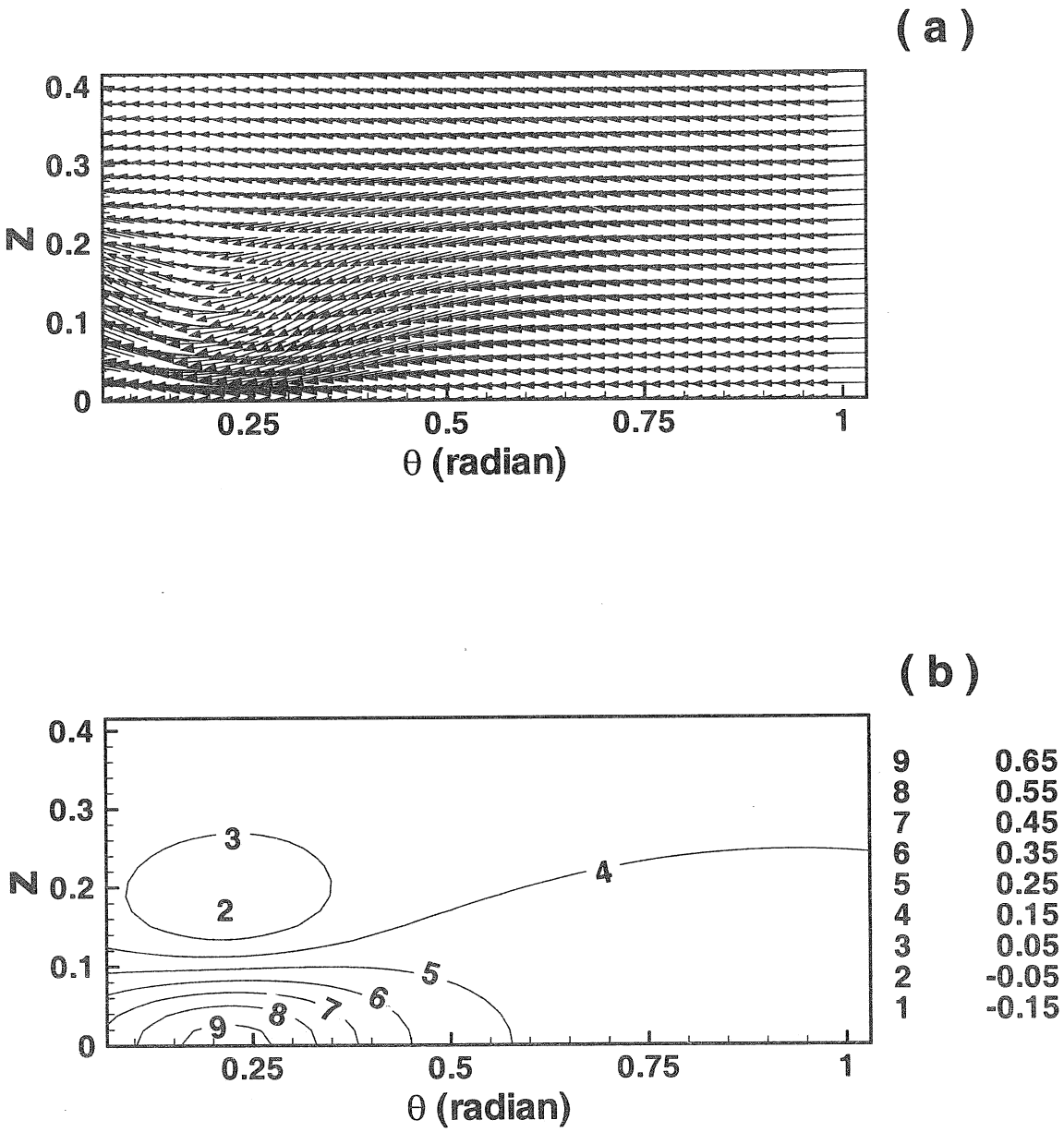

Figure 13: Same as figure 6 for the theoretical model.

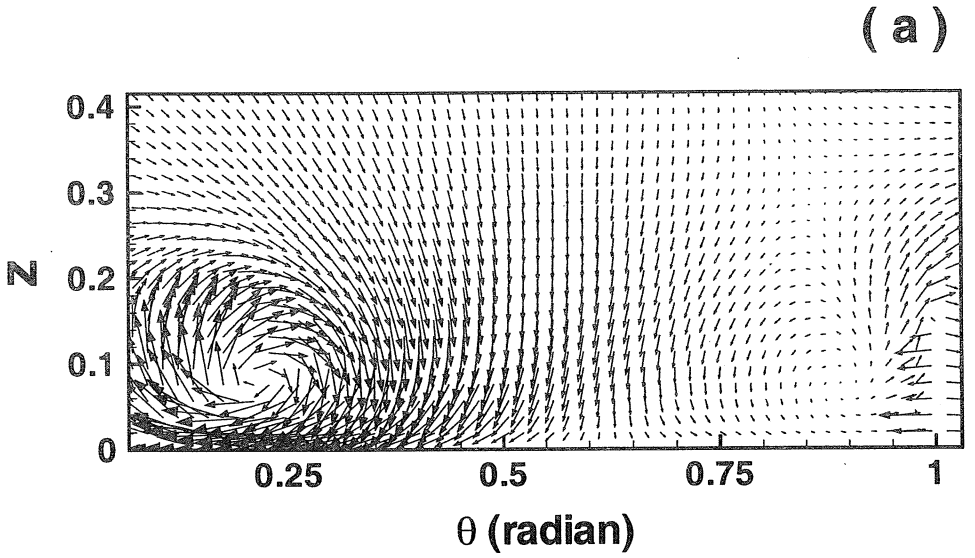

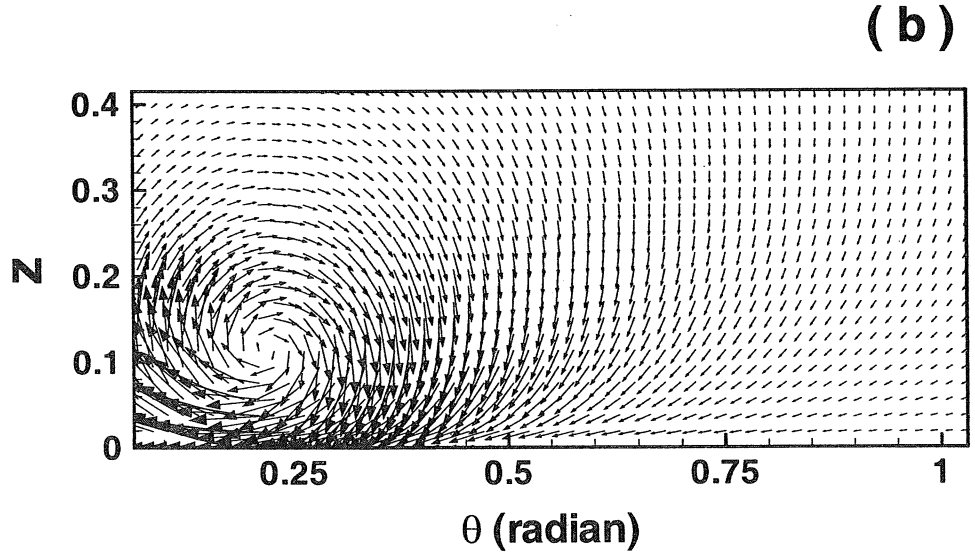

Figure 14: A closer comparison of the tip vortex field after subtraction of the jet component. (a) experimental measurement and (b) the theoretical model. Noise in the experimental measurement near the lower right hand corner is due to blade reflection.

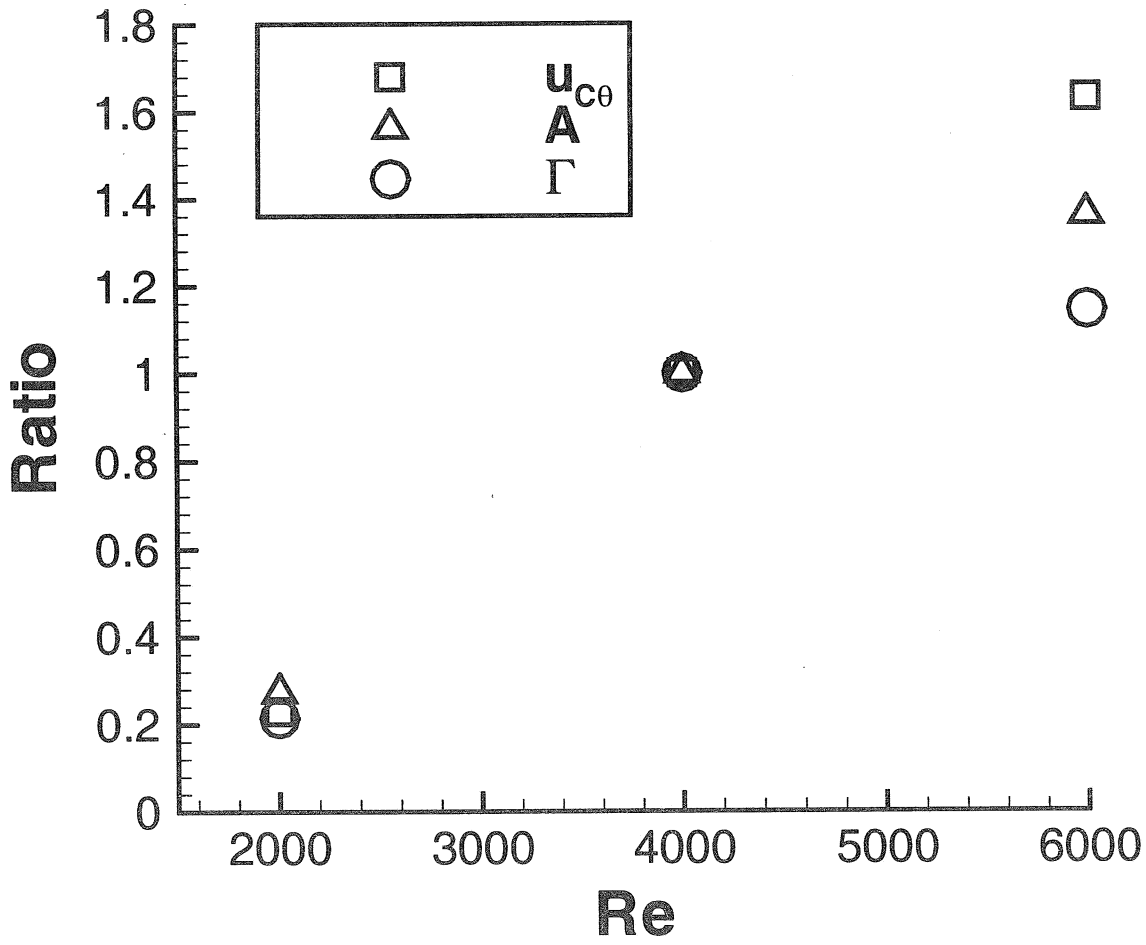

Figure 15: Scaling of circumferential flow, jet strength (A) and circulation of the tip vortex pair (Γ) with Re. All three quantities are plotted as a ratio with respected to their value at the intermediate Reynolds number of 4000 corresponding to 100 rpm.

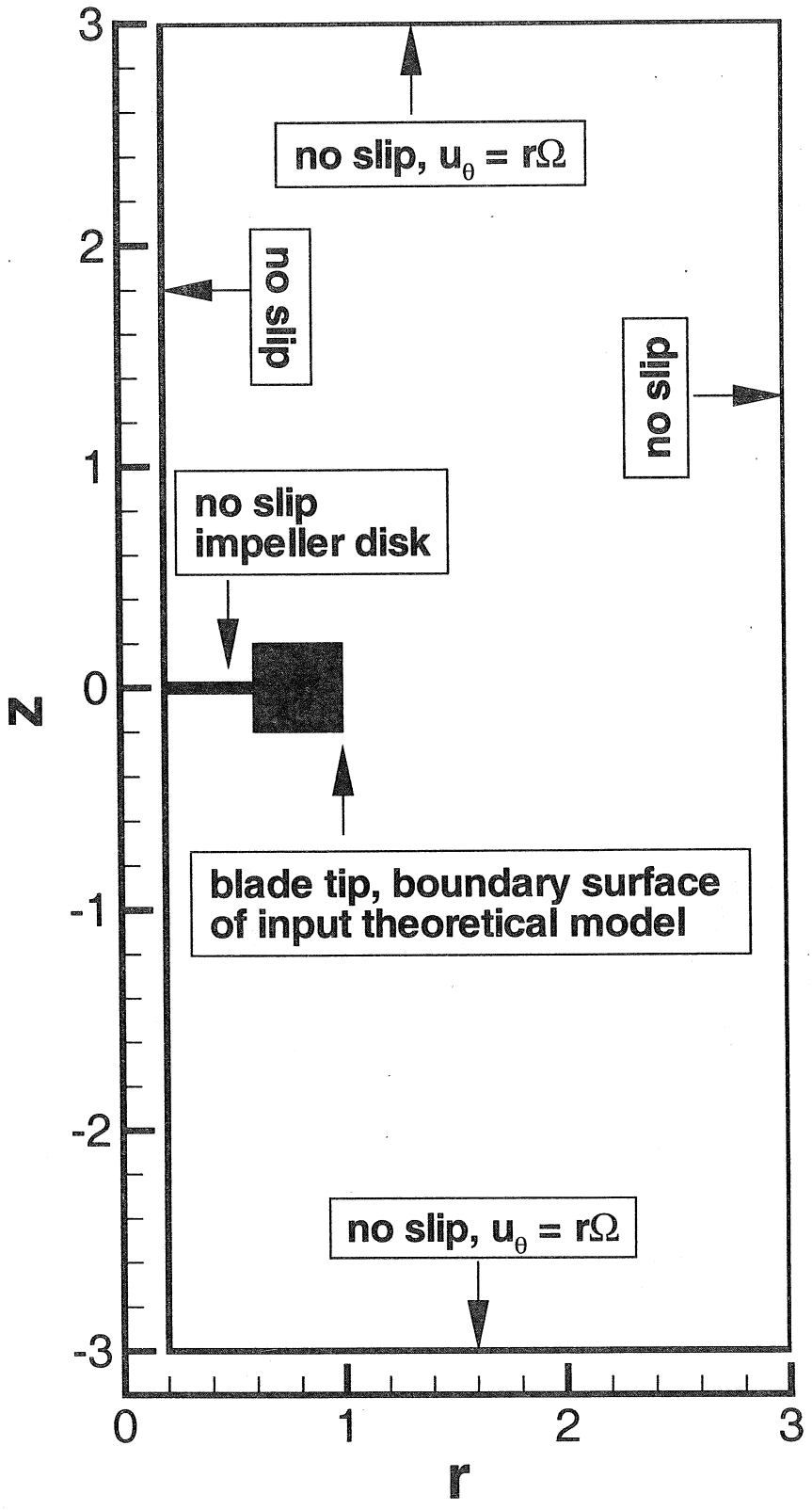

Figure 16: Schematic of the overall computational geometry in the $r-z$ plane and the boundary conditions.

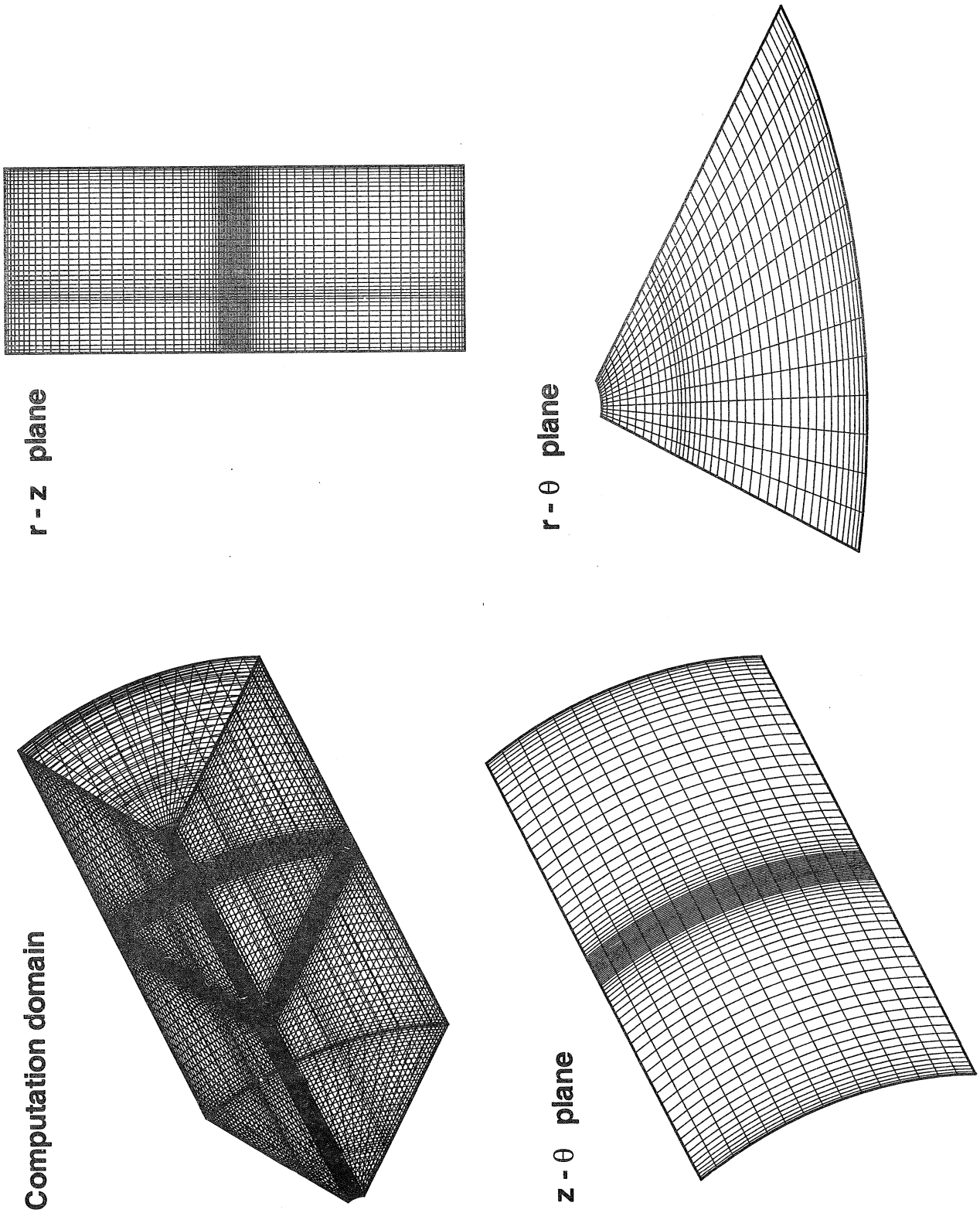

Figure 17: Computational non-uniform grid with grid clustering near the impeller region used to better resolve the complex flow near the impeller.

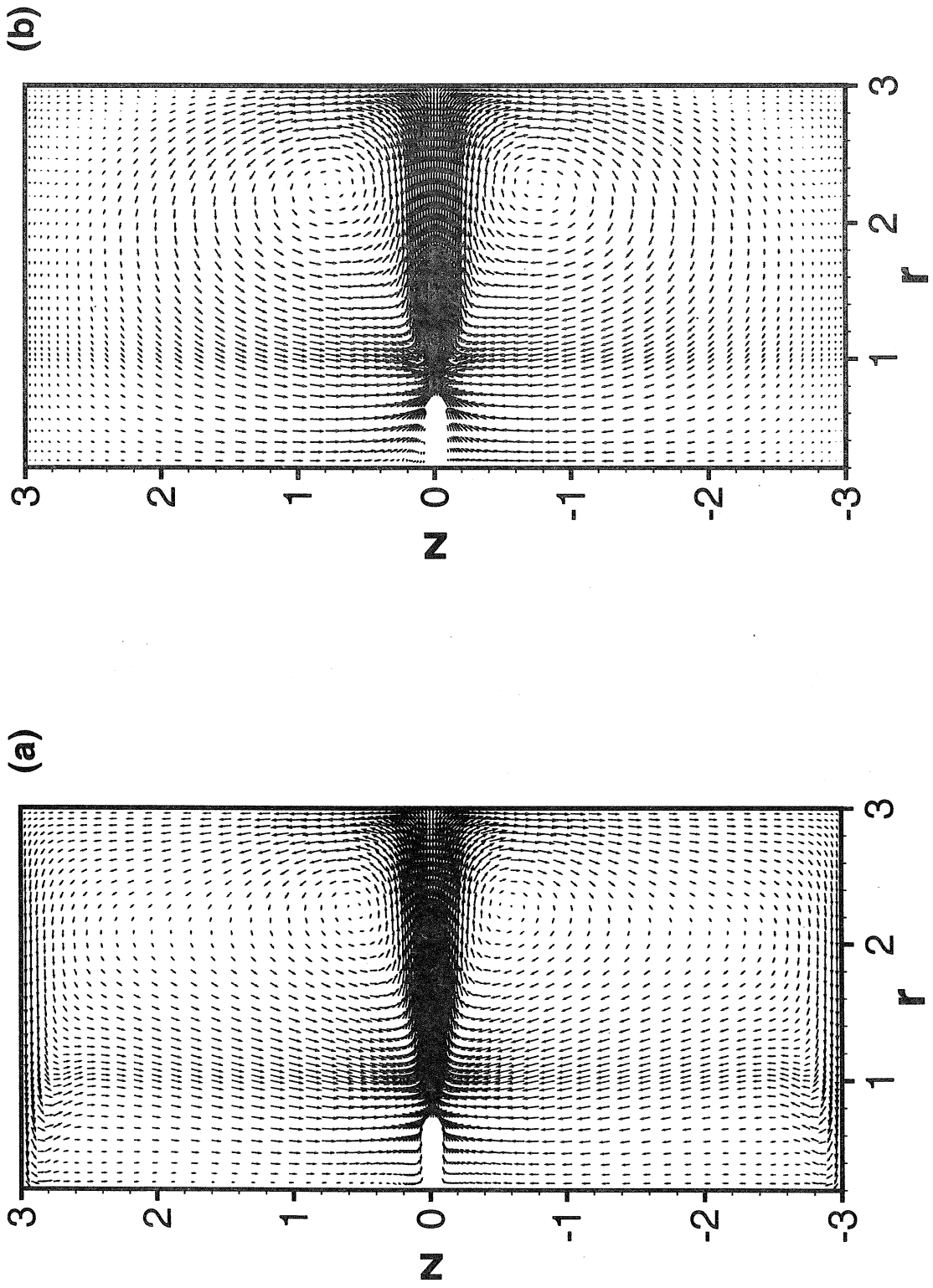

Figure 18: Velocity vector plot on the $r-z$ plane computed from (a) the three-dimensional and (b) the two-dimensional simulations. In the case of the three-dimensional simulation, the θ-averaged flow is plotted.

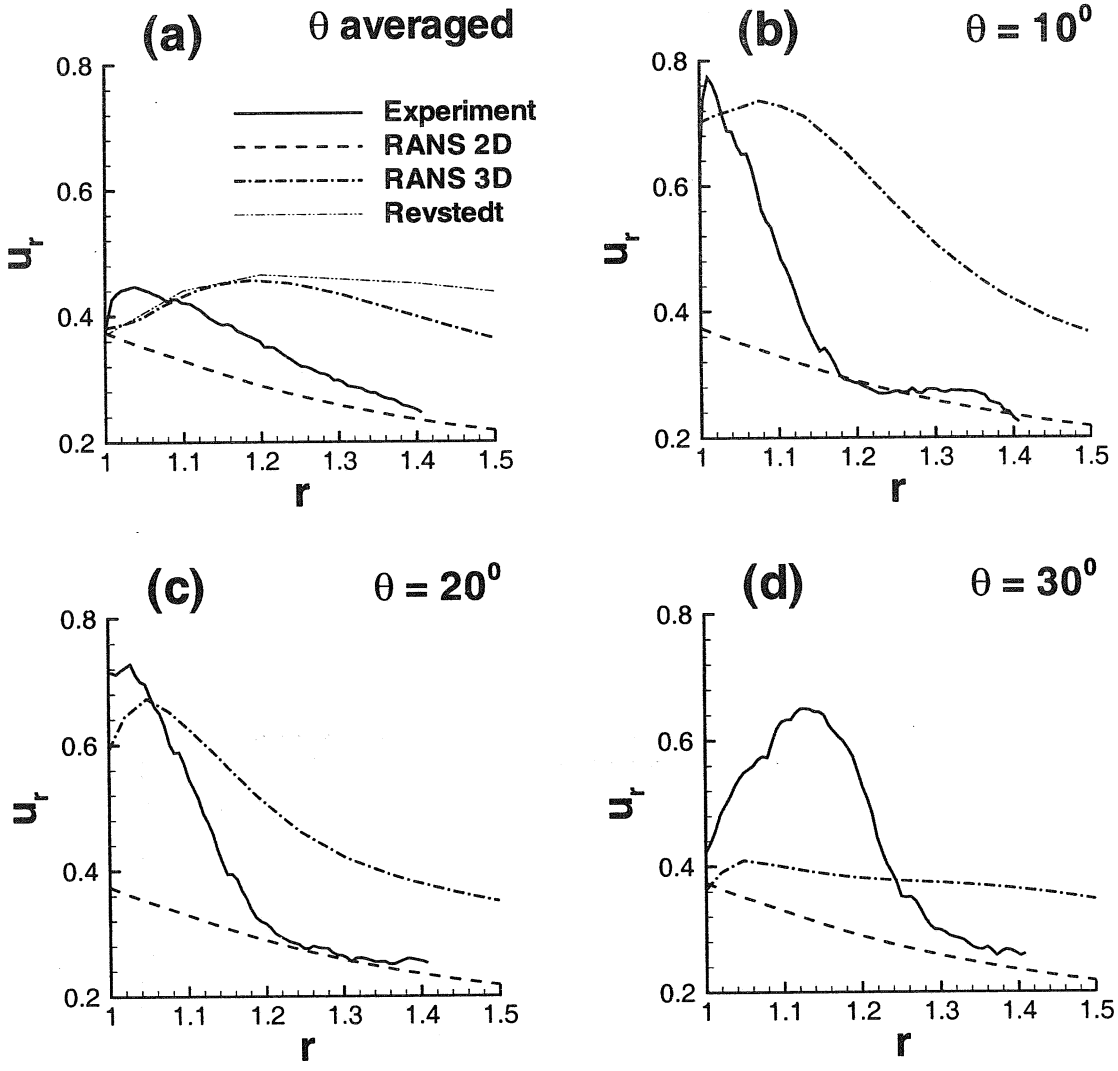

Figure 19: Comparison of the radial velocity profile along the tank centerline at $z = 0$. The 3D results are compared with the experimental measurement and also with the 2D simulation and the results of Revstedt *et al.* (1998). (a) θ-averaged profile, (b) $\theta = 10°$, (c) 20° and (d) 30°.

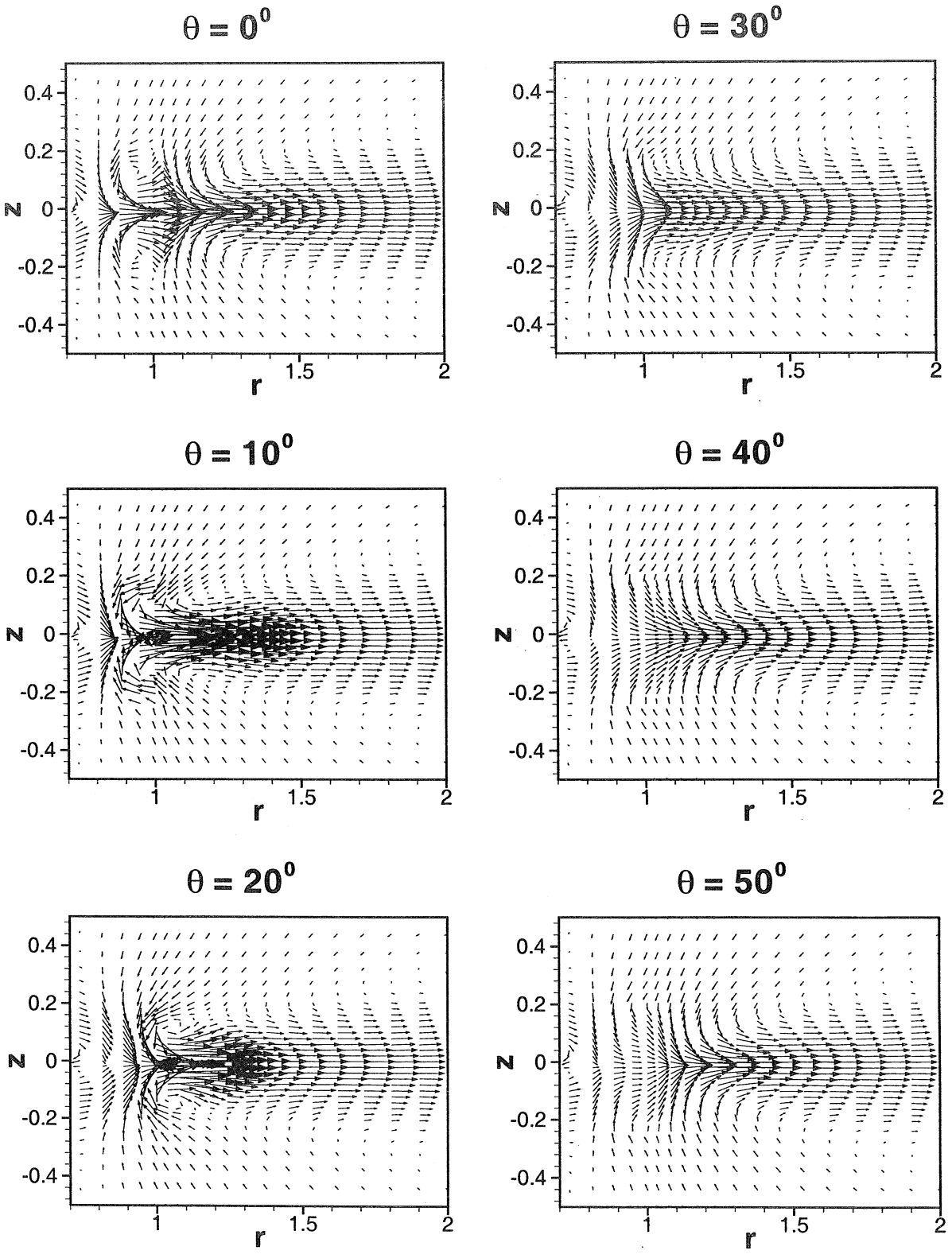

Figure 20: Velocity vector plot from the three-dimensional simulation at various azimuthal locations in the region close to the impeller swept volume. (a) $\theta = 0°$, (b) 10°, (c) 20°,
(d) 30°, (e) 40°, and (f) 50°.

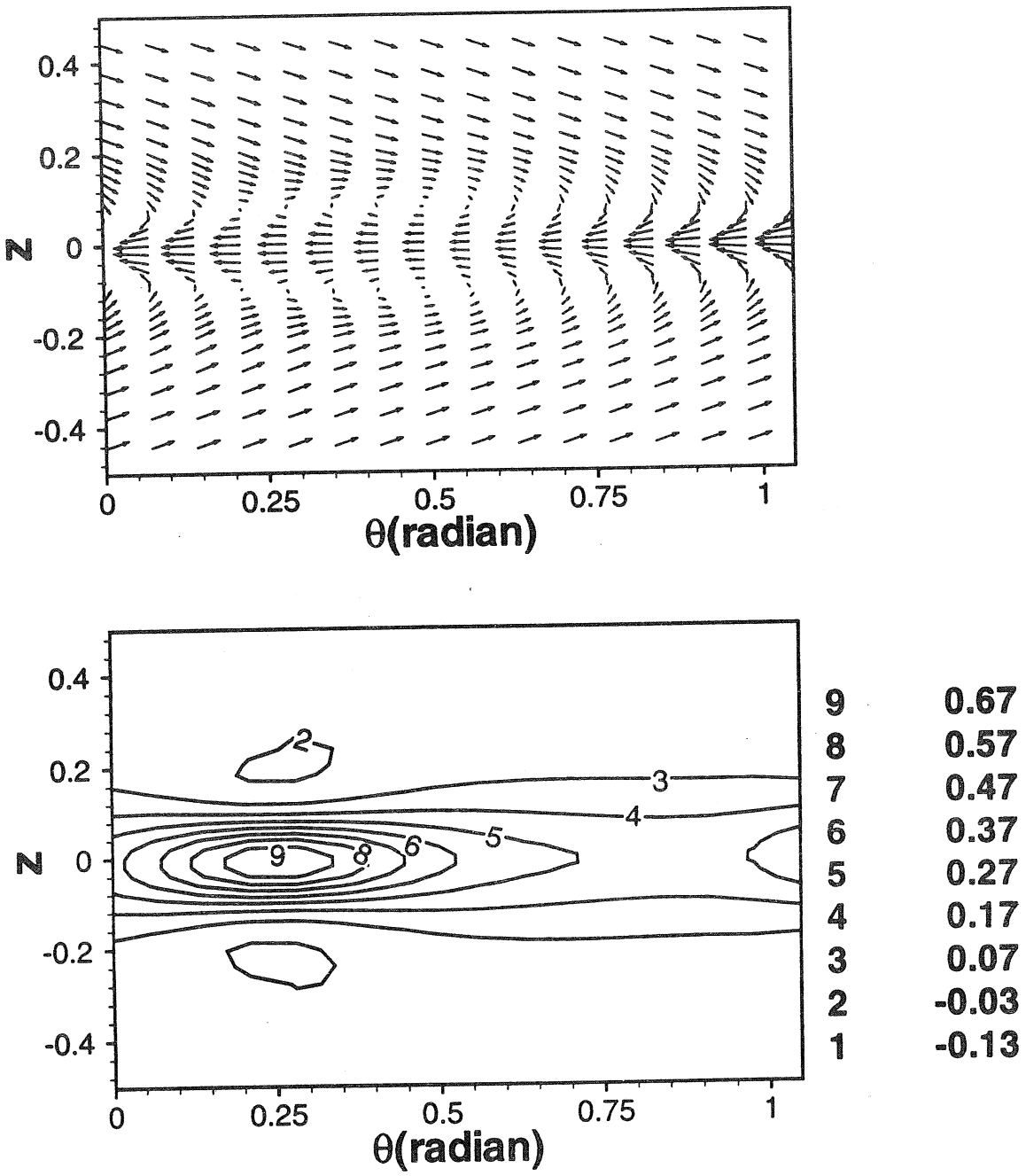

Figure 21: The in-plane velocity vector on a $\theta - z$ plane located at $r = 1$. 1 obtained from the three-dimensional simulation.

List of Recent TAM Reports

No.	Authors	Title	Date
843	Fang, B., F. L. Carranza, and R. B. Haber	An adaptive discontinuous Galerkin method for viscoplastic analysis—*Computer Methods in Applied Mechanics and Engineering* **150**, 191–198 (1997)	Jan. 1997
844	Xu, S., T. D. Aslam, and D. S. Stewart	High-resolution numerical simulation of ideal and non-ideal compressible reacting flows with embedded internal boundaries—*Combustion Theory and Modeling* **1**, 113–142 (1997)	Jan. 1997
845	Zhou, J., C. D. Meinhart, S. Balachandar, and R. J. Adrian	Formation of coherent hairpin packets in wall turbulence—In *Self-Sustaining Mechanisms in Wall Turbulence*, R. L. Panton, ed. Southampton, UK: Computational Mechanics Publications, 109–134 (1997)	Feb. 1997
846	Lufrano, J. M., P. Sofronis, and H. K. Birnbaum	Elastoplastically accommodated hydride formation and embrittlement—*Journal of Mechanics and Physics of Solids*, **46**, 1497–1520 (1998)	Feb. 1997
847	Keane, R. D., N. Fujisawa, and R. J. Adrian	Unsteady non-penetrative thermal convection from non-uniform surfaces—In *Geophysical and Astrophysical Convection*, R. Kerr, ed. (1997)	Feb. 1997
848	Aref, H., and M. Brøns	On stagnation points and streamline topology in vortex flows—*Journal of Fluid Mechanics* **370**, 1–27 (1998)	Mar. 1997
849	Asghar, S., T. Hayat, and J. G. Harris	Diffraction by a slit in an infinite porous barrier—*Wave Motion*, **30**, 96–104 (1998)	Mar. 1997
850	Shawki, T. G., H. Aref, and J. W. Phillips	Mechanics on the Web—Proceedings of the International Conference on Engineering Education (Aug. 1997, Chicago)	Apr. 1997
851	Stewart, D. S., and J. Yao	The normal detonation shock velocity–curvature relationship for materials with non-ideal equation of state and multiple turning points—*Combustion* **113**, 224–235 (1998)	Apr. 1997
852	Fried, E., A. Q. Shen, and S. T. Thoroddsen	Wave patterns in a thin layer of sand within a rotating horizontal cylinder—*Physics of Fluids* **10**, 10–12 (1998)	Apr. 1997
853	Boyland, P. L., H. Aref, and M. A. Stremler	Topological fluid mechanics of stirring—*Bulletin of the American Physical Society* **41**, 1683 (1996)	Apr. 1997
854	Parker, S. J., and S. Balachandar	Viscous and inviscid instabilities of flow along a streamwise corner—*Bulletin of the American Physical Society* **42**, 2155 (1997)	May 1997
855	Soloff, S. M., R. J. Adrian, and Z.-C. Liu	Distortion compensation for generalized stereoscopic particle image velocimetry—*Measurement Science and Technology* **8**, 1–14 (1997)	May 1997
856	Zhou, Z., R. J. Adrian, S. Balachandar, and T. M. Kendall	Mechanisms for generating coherent packets of hairpin vortices in near-wall turbulence—*Bulletin of the American Physical Society* **42**, 2243 (1997)	June 1997
857	Neishtadt, A. I., D. L. Vainshtein, and A. A. Vasiliev	Chaotic advection in a cubic stokes flow—*Physica D* **111**, 227 (1997).	June 1997
858	Weaver, R. L.	Ultrasonics in an aluminum foam—*Ultrasonics* **36**, 435–442 (1998)	July 1997
859	Riahi, D. N.	High gravity convection in a mushy layer during alloy solidification—In *Nonlinear Instability, Chaos and Turbulence*, D. N. Riahi and L. Debnath, eds., **1**, 301–336 (1998)	July 1997
860	Najjar, F. M., and S. Balachandar	Low-frequency unsteadiness in the wake of a normal plate, *Bulletin of the American Physical Society* **42**, 2212 (1997)	Aug. 1997
861	Short, M.	A parabolic linear evolution equation for cellular detonation instability—*Combustion Theory and Modeling* **1**, 313–346 (1997)	Aug. 1997
862	Short, M., and D. S. Stewart	Cellular detonation stability, I: A normal-mode linear analysis—*Journal of Fluid Mechanics* **368**, 229–262 (1998)	Sept. 1997
863	Carranza, F. L., and R. B. Haber	A numerical study of intergranular fracture and oxygen embrittlement in an elastic–viscoplastic solid—*Journal of the Mechanics and Physics of Solids*, **47**, 27–58 (1997)	Oct. 1997
864	Sakakibara, J., and R. J. Adrian	Whole-field measurement of temperature in water using two-color laser-induced fluorescence—*Experiments in Fluids* **26**, 7–15 (1999)	Oct. 1997

List of Recent TAM Reports (cont'd)

No.	Authors	Title	Date
865	Riahi, D. N.	Effect of surface corrugation on convection in a three-dimensional finite box of fluid-saturated porous material—*Theoretical and Computational Fluid Dynamics*, 13, 189-208 (1999)	Oct. 1997
866	Baker, C. F., and D. N. Riahi	Three-dimensional flow instabilities during alloy solidification—*Bulletin of the American Physical Society* **41**, 1699 (1998)	Oct. 1997
867	Fried, E.	Introduction (only) to *The Physical and Mathematical Foundations of the Continuum Theory of Evolving Phase Interfaces* (book containing 14 seminal papers dedicated to Morton E. Gurtin), Berlin: Springer-Verlag, in press (1998)	Oct. 1997
868	Folguera, A., and J. G. Harris	Coupled Rayleigh surface waves in a slowly varying elastic waveguide—*Proceedings of the Royal Society of London A* **455**, 917–931 (1998)	Oct. 1997
869	Stewart, D. S.	Detonation shock dynamics: Application for precision cutting of metal with detonation waves	Oct. 1997
870	Shrotriya, P., and N. R. Sottos	Creep and relaxation behavior of woven glass/epoxy substrates for multilayer circuit board applications—*Polymer Composites* **19**, 567–578 (1998)	Nov. 1997
871	Riahi, D. N.	Boundary wave–vortex interaction in channel flow at high Reynolds numbers, *Fluid Dynamics Research* **25**, 129–145 (1999)	Nov. 1997
872	George, W. K., L. Castillo, and M. Wosnik	A theory for turbulent pipe and channel flows—paper presented at *Disquisitiones Mechanicae* (Urbana, Ill., October 1996)	Nov. 1997
873	Aslam, T. D., and D. S. Stewart	Detonation shock dynamics and comparisons with direct numerical simulation—*Combustion Theory and Modeling* **3**, 77–101 (1999)	Dec. 1997
874	Short, M., and A. K. Kapila	Blow-up in semilinear parabolic equations with weak diffusion *Combustion Theory and Modeling* **2**, 283-291 (1998)	Dec. 1997
875	Riahi, D. N.	Analysis and modeling for a turbulent convective plume—*Mathematical and Computer Modeling* **28**, 57–63 (1998)	Jan. 1998
876	Stremler, M. A., and H. Aref	Motion of three point vortices in a periodic parallelogram—*Journal of Fluid Mechanics* **392**, 101-128 (1999)	Feb. 1998
877	Dey, N., K. J. Hsia, and D. F. Socie	On the stress dependence of high-temperature static fatigue life of ceramics	Feb. 1998
878	Brown, E. N., and N. R. Sottos	Thermoelastic properties of plain weave composites for multilayer circuit board applications	Feb. 1998
879	Riahi, D. N.	On the effect of a corrugated boundary on convective motion—*Journal of Theoretical and Applied Mechanics*, in press (1999)	Feb. 1998
880	Riahi, D. N.	On a turbulent boundary layer flow over a moving wavy wall	Mar. 1998
881	Riahi, D. N.	Vortex formation and stability analysis for shear flows over combined spatially and temporally structured walls—*Mathematical Problems in Engineering* **5**, 317–328 (1999)	June 1998
882	Short, M., and D. S. Stewart	The multi-dimensional stability of weak heat release detonations—*Journal of Fluid Mechanics* **382**, 109–135 (1999)	June 1998
883	Fried, E., and M. E. Gurtin	Coherent solid-state phase transitions with atomic diffusion: A thermomechanical treatment—*Journal of Statistical Physics* **95**, 1361–1427 (1999)	June 1998
884	Langford, J. A., and R. D. Moser	Optimal large-eddy simulation formulations for isotropic turbulence—*Journal of Fluid Mechanics* **398**, 321–346 (1999)	July 1998
885	Riahi, D. N.	Boundary-layer theory of magnetohydrodynamic turbulent convection—*Proceedings of the Indian National Academy (Physical Science)* **65A**, 109–116 (1999)	Aug. 1998
886	Riahi, D. N.	Nonlinear thermal instability in spherical shells—in *Nonlinear Instability, Chaos and Turbulence* **2**, 377–402 (1999)	Aug. 1998
887	Riahi, D. N.	Effects of rotation on fully non-axisymmetric chimney convection during alloy solidification—*Journal of Crystal Growth* **204**, 382–394 (1999)	Sept. 1998

List of Recent TAM Reports (cont'd)

No.	Authors	Title	Date
888	Fried, E., and S. Sellers	The Debye theory of rotary diffusion	Sept. 1998
889	Short, M., A. K. Kapila, and J. J. Quirk	The hydrodynamic mechanisms of pulsating detonation wave instability—*Proceedings of the Royal Society of London, A* **357**, 3621–3638 (1999)	Sept. 1998
890	Stewart, D. S.	The shock dynamics of multidimensional condensed and gas phase detonations—Proceedings of the 27th International Symposium on Combustion (Boulder, Colo.)	Sept. 1998
891	Kim, K. C., and R. J. Adrian	Very large-scale motion in the outer layer—*Physics of Fluids* **2**, 417–422 (1999)	Oct. 1998
892	Fujisawa, N., and R. J. Adrian	Three-dimensional temperature measurement in turbulent thermal convection by extended range scanning liquid crystal thermometry—*Journal of Visualization* **1**, 355-364 (1999)	Oct. 1998
893	Shen, A. Q., E. Fried, and S. T. Thoroddsen	Is segregation-by-particle-type a generic mechanism underlying finger formation at fronts of flowing granular media?—*Particulate Science and Technology* **17**, 141–148 (1999)	Oct. 1998
894	Shen, A. Q.	Mathematical and analog modeling of lava dome growth	Oct. 1998
895	Buckmaster, J. D., and M. Short	Cellular instabilities, sub-limit structures, and edge-flames in premixed counterflows—*Combustion Theory and Modeling* **3**, 199–214 (1999)	Oct. 1998
896	Harris, J. G.	*Elastic waves*—Part of a book to be published by Cambridge University Press	Dec. 1998
897	Paris, A. J., and G. A. Costello	Cord composite cylindrical shells	Dec. 1998
898	Students in TAM 293–294	Thirty-fourth student symposium on engineering mechanics (May 1997), J. W. Phillips, coordinator: Selected senior projects by M. R. Bracki, A. K. Davis, J. A. (Myers) Hommema, and P. D. Pattillo	Dec. 1998
899	Taha, A., and P. Sofronis	A micromechanics approach to the study of hydrogen transport and embrittlement	Jan. 1999
900	Ferney, B. D., and K. J. Hsia	The influence of multiple slip systems on the brittle–ductile transition in silicon—*Materials Science Engineering A* **272**, 422–430 (1999)	Feb. 1999
901	Fried, E., and A. Q. Shen	Supplemental relations at a phase interface across which the velocity and temperature jump	Mar. 1999
902	Paris, A. J., and G. A. Costello	Cord composite cylindrical shells: Multiple layers of cords at various angles to the shell axis	Apr. 1999
903	Ferney, B. D., M. R. DeVary, K. J. Hsia, and A. Needleman	Oscillatory crack growth in glass—*Scripta Materialia* **41**, 275–281 (1999)	Apr. 1999
904	Fried, E., and S. Sellers	Microforces and the theory of solute transport	Apr. 1999
905	Balachandar, S., J. D. Buckmaster, and M. Short	The generation of axial vorticity in solid-propellant rocket-motor flows	May 1999
906	Aref, H., and D. L. Vainchtein	The equation of state of a foam	May 1999
907	Subramanian, S. J., and P. Sofronis	Modeling of the interaction between densification mechanisms in powder compaction	May 1999
908	Aref, H., and M. A. Stremler	Four-vortex motion with zero total circulation and impulse—*Physics of Fluids* **11**, 3704-3715	May 1999
909	Adrian, R. J., K. T. Christensen, and Z.-C. Liu	On the analysis and interpretation of turbulent velocity fields—*Experiments in Fluids*, in press (1999)	May 1999
910	Fried, E., and S. Sellers	Theory for atomic diffusion on fixed and deformable crystal lattices	June 1999

List of Recent TAM Reports (cont'd)

No.	Authors	Title	Date
911	Sofronis, P., and N. Aravas	Hydrogen induced shear localization of the plastic flow in metals and alloys	June 1999
912	Anderson, D. R., D. E. Carlson, and E. Fried	A continuum-mechanical theory for nematic elastomers	June 1999
913	Riahi, D. N.	High Rayleigh number convection in a rotating melt during alloy solidification—*Recent Developments in Crystal Growth Research*, in press (2000)	July 1999
914	Riahi, D. N.	Buoyancy driven flow in a rotating low Prandtl number melt during alloy solidification—*Current Topics in Crystal Growth Research*, in press (2000)	July 1999
915	Adrian, R. J.	On the physical space equation for large-eddy simulation of inhomogeneous turbulence	July 1999
916	Riahi, D. N.	Wave and vortex generation and interaction in turbulent channel flow between wavy boundaries	July 1999
917	Boyland, P. L., M. A. Stremler, and H. Aref	Topological fluid mechanics of point vortex motions	July 1999
918	Riahi, D. N.	Effects of a vertical magnetic field on chimney convection in a mushy layer—*Journal of Crystal Growth*, in press (2000)	Aug. 1999
919	Riahi, D. N.	Boundary mode–vortex interaction in turbulent channel flow over a non-wavy rough wall	Sept. 1999
920	Block, G. I., J. G. Harris, and T. Hayat	Measurement models for ultrasonic nondestructive evaluation	Sept. 1999
921	Zhang, S., and K. J. Hsia	Modeling the fracture of a sandwich structure due to cavitation in a ductile adhesive layer	Sept. 1999
922	Nimmagadda, P. B. R., and P. Sofronis	Leading order asymptotics at sharp fiber corners in creeping-matrix composite materials	Oct. 1999
923	Yoo, S., and D. N. Riahi	Effects of a moving wavy boundary on channel flow instabilities	Nov. 1999
924	Adrian, R. J., C. D. Meinhart, and C. D. Tomkins	Vortex organization in the outer region of the turbulent boundary layer	Nov. 1999
925	Riahi, D. N., and A. T. Hsui	Finite amplitude thermal convection with variable gravity	Dec. 1999
926	Kwok, W. Y., R. D. Moser, and J. Jiménez	A critical evaluation of the resolution properties of *B*-spline and compact finite difference methods	Feb. 2000
927	Ferry, J. P., and S. Balachandar	A fast Eulerian method for two-phase flow	Feb. 2000
928	Thoroddsen, S. T., and K. Takehara	The coalescence–cascade of a drop	Feb. 2000
929	Liu, Z.-C., R. J. Adrian, and T. J. Hanratty	Large-scale modes of turbulent channel flow: Transport and structure	Feb. 2000
930	Borodai, S. G., and R. D. Moser	The numerical decomposition of turbulent fluctuations in a compressible boundary layer	Mar. 2000
931	Balachandar, S., and F. M. Najjar	Optimal two-dimensional models for wake flows	Mar. 2000
932	Yoon, H. S., K. V. Sharp, D. F. Hill, R. J. Adrian, S. Balachandar, M. Y. Ha, and K. Kar	Integrated experimental and computational approach to simulation of flow in a stirred tank	Mar. 2000